



저작자표시-비영리-변경금지 2.0 대한민국

이용자는 아래의 조건을 따르는 경우에 한하여 자유롭게

- 이 저작물을 복제, 배포, 전송, 전시, 공연 및 방송할 수 있습니다.

다음과 같은 조건을 따라야 합니다:



저작자표시. 귀하는 원저작자를 표시하여야 합니다.



비영리. 귀하는 이 저작물을 영리 목적으로 이용할 수 없습니다.



변경금지. 귀하는 이 저작물을 개작, 변형 또는 가공할 수 없습니다.

- 귀하는, 이 저작물의 재이용이나 배포의 경우, 이 저작물에 적용된 이용허락조건을 명확하게 나타내어야 합니다.
- 저작권자로부터 별도의 허가를 받으면 이러한 조건들은 적용되지 않습니다.

저작권법에 따른 이용자의 권리는 위의 내용에 의하여 영향을 받지 않습니다.

이것은 [이용허락규약\(Legal Code\)](#)을 이해하기 쉽게 요약한 것입니다.

[Disclaimer](#)

공학박사 학위논문

Generation of charged Ag
nanoparticles and their
contribution to film growth during
DC magnetron sputtering

DC 마그네트론 스퍼터링 공정 중 생성된 하전된
은 나노 입자와 그들이 박막 성장에 미치는 영향

2021 년 2 월

서울대학교 대학원

재료공학부

장 길 수

Generation of charged Ag nanoparticles and their contribution to film growth during DC magnetron sputtering

지도교수 황 농 문

이 논문을 공학박사 학위논문으로 제출함

2021 년 2월

서울대학교 대학원

재료공학부

장 길 수

장길수의 공학박사 학위논문을 인준함
2021년 2월

위원장	박 은 수	(인)
부위원장	황 농 문	(인)
위원	장 호 원	(인)
위원	김 근 수	(인)
위원	나 태 옥	(인)

Abstract

Generation of charged Ag nanoparticles and their contribution to film growth during DC magnetron sputtering

Gil-Su Jang

Department of Materials Science and Engineering

The Graduate School

Seoul National University

The possibility that charged nanoparticles (CNPs) are generated in the gas phase during direct current (DC) magnetron sputtering of Ag is studied. Sputtered Ag particles could be captured on an ultrathin amorphous carbon membrane for transmission electron microscopy (TEM) observation. It is confirmed that the average particle size and the total area of deposition under the condition of the positive bias applied to the substrate are bigger than those under the condition of the negative bias applied to the substrate. The results indicate that some of the sputtered Ag particles are negatively charged. To evaluate the contribution of negatively-charged

particles to the film growth, Ag thin films were deposited for 30 min on the Si substrate with the substrate biases of -300 , 0 and $+300$ V and analyzed by field-emission scanning electron microscopy (FESEM), X-ray diffraction (XRD) and four-point probe. When $+300$ V was applied to the substrate, the film growth rate was highest with the film thickness of 85.0 nm, the crystallinity was best with the smallest full width at half maximum (FWHM) value of 0.44 and the resistivity was smallest with $3.67 \mu\Omega \cdot \text{cm}$. In contrast, when -300 V was applied to the substrate, the film growth rate was lowest with the film thickness of 68.9 nm, the crystallinity was worst with the largest FWHM value of 0.53 and the resistivity was largest with $8.87 \mu\Omega \cdot \text{cm}$. This result indicates that the charge plays an important role in film growth and can be a new process parameter in sputtering.

To study the effect of process parameters on charged nanoparticles, the effects of sputtering power on the deposition rate and microstructure, crystallinity, and electrical properties of Ag films during direct current (DC) magnetron sputtering are investigated. Thin films (~ 100 nm) are deposited at sputtering powers of 10 , 20 , 50 , 100 , 200 and 300 W and analyzed by field-emission scanning

electron microscopy (FESEM), X-ray diffraction (XRD), transmission electron microscopy (TEM) and a four-point probe. The film deposited at a sputtering power of 10 W has the lowest growth rate, but the highest crystalline quality, with the lowest full width at half maximum (FWHM) and the lowest resistivity. The film deposited at a sputtering power of 200 W has the highest growth rate, and the second best crystalline quality with an FWHM and resistivity. The film deposited at a sputtering power of 50 W has the moderate growth rate, and the worst crystalline quality with an FWHM and resistivity. High-resolution TEM observations reveal that films deposited at sputtering powers of 10 and 200 W have far fewer defects, such as grain boundaries, dislocations and stacking faults, compared to films deposited at a sputtering power of 50 W. Such deposition behavior could be explained by sputtering power is affected by generating the charged nanoparticles. And the good quality of film could be obtained under conditions of high deposition rate, and charge plays an important role.

And, the effects of DC magnetron sputtering working pressure on the thickness, the crystallinities, and electrical properties of Ag thin films are investigated. Thin films are deposited while biasing the

substrates of -300 , 0 and $+300$ V for 30 minutes at each plasma power of 20, 50, 100 and 200 W and working pressures of 2.5, 5, 10, and 20 mTorr. In all sputtering power conditions, as the working pressure decreased, the growth rate of the thin film increased and the proportion of charged nanoparticles increased. The growth rate increased due to the positive bias applied to the substrate, and the growth rate decreased due to the negative bias. The FWHM of Ag (111) peaks obtained through XRD analysis showed different patterns according to substrate bias as the process pressure decreased. It decreased when a positive bias was applied to the substrate, and increased when a negative bias was applied. Resistivity showed the same pattern as the change of the FWHM of Ag (111) peaks. This change in the deposition behavior of the Ag film can be understood as the effect of the charged nanoparticles. The working pressure affected the sputtered nanoparticle size and changed the possibility of the particle being charged.

Keyword: DC magnetron sputtering, Ag, charged nanoparticles, substrate bias, sputtering power, working pressure, thin film

Student Number: 2014-21465

List of Figures

Figure 1.1 explanation of classical and non-classical crystallization.

Figure 1.2. FESEM images of (a) cubic diamond deposited on the Si substrate and (b) carbon soot deposited on the Fe substrate.

Figure 2.1 (a) Schematic of the DC sputtering system and (b) the current measured on the substrate holder.

Figure 2.2. TEM images of Ag particles captured on an amorphous carbon membrane at the substrate bias of 0 V for (a) 1 s, (b) 3 s, (c) 5 s, (d) 7 s and (e) 10 s.

Figure 2.3. HRTEM image and FFT information (inset of the lower right in the image) of Ag sputtered particles captured on an amorphous carbon membrane at the substrate bias of 0 V for (a) 1 s and (b) 10 s.

Figure 2.4. TEM images of Ag particles captured on an amorphous carbon membrane at the substrate bias of +300 V for (a) 1 s; (b) 3

s; (c) 5 s; (d) 7 s; and (e) 10 s.

Figure 2.5. TEM images of Ag particles captured on an amorphous carbon membrane at the substrate bias of -300 V for (a) 1 s; (b) 3 s; (c) 5 s; (d) 7 s; and (e) 10 s.

Figure 2.6. Plots of (a) particle average diameter; (b) particle count per μm^2 ; and (c) total area of Ag particle per μm^2 against the capture time analyzed by the ImageJ program.

Figure 2.7. Cross-section FESEM images of the Ag films deposited on Si substrates at the electric biases of (a) -300 V; (b) 0 V; and (c) +300 V.

Figure 2.8. Top-view FESEM images of ((a)~(c)) low magnification and ((d)~(f)) high magnification of the Ag films deposited on Si substrates at the electric biases of ((a) and (d)) -300 V ((b) and (e)) 0 V and ((c) and (f)) +300 V.

Figure 2.9. XRD data of the Ag films deposited at the electric biases of -300, 0 and +300 V in the 2θ range of 35° - 50° . The FWHMs of

(111) peaks for -300, 0 and +300 V are 0.53, 0.47 and 0.44, respectively.

Figure 2.10. Resistivity of the Ag films deposited at the electric biases of -300, 0 and +300 V.

Figure 2.11. Gaussian graph for Ag nanoparticles size distribution under each capture condition.

Figure 3.1. Schematic of DC magnetron sputtering chamber.

Figure 3.2. Cross-sectional FESEM images of Ag films deposited on Si substrates at sputtering powers of (a) 10 W (b) 20 W (c) 50 W (d) 100 W (e) 200 W and (f) 300 W.

Figure 3.3. Top-view FESEM images of the Ag films deposited on Si substrates at sputtering power of (a) 10 W (b) 20 W (c) 50 W (d) 100 W (e) 200 W and (f) 300 W.

Figure 3.4. XRD data of the Ag films deposited at the sputtering power of 10, 20, 50, 100, 200 and 300 W in the 2θ range of 35° – 50° .

Figure 3.5. Resistivity of the Ag films deposited at the sputtering power of 10, 20, 50, 100, 200 and 300 W.

Figure 3.6. Low-magnification TEM images of Ag films deposited on Si substrates at sputtering powers of (a) 10 W (b) 50 W and (c) 200 W.

Figure 3.7. HRTEM and FFT images of Ag films deposited on Si substrates at sputtering power of (a) 10 W (b) 50 W and (c) 200 W. The triangle mark is a peak of 4H-Ag HCP and the circle mark is a peak of 3C-Ag FCC in FFT images.

Figure 3.8. Summary of structural parameters of the 3C and 4H modifications of silver.

Figure 3.9. Cross-sectional FESEM images of Ag films deposited on Si substrates at the electric biases of (a) -300 V (b) 0 V and (c) +300 V with a sputtering power of 10 W.

Figure 3.10. Cross-sectional FESEM images of Ag films deposited on Si substrates at the electric biases of (a) -300 V (b) 0 V and (c)

+300 V with a sputtering power of 200 W.

Figure 4.1. (a) Schematic of the DC magnetron sputtering chamber and (b) the current measured on the substrate holder at the plasma power of 100 W.

Figure 4.2. Cross-section FESEM images of the Ag films deposited on Si substrates at the working pressure of (a) 2.5 mTorr; (b) 5 mTorr; (c) 10 mTorr; and (d) 20 mTorr at the sputtering power of 100 W.

Figure 4.3. Cross-section FESEM images of the Ag films deposited on Si substrates at the electric biases of (a) -300 V; (b) 0 V; and (c) +300 V at the working pressure of 2.5 mTorr and the sputtering power of 100 W.

Figure 4.4. Plots of the thickness of Ag films according to the working pressure change while applying a bias to the substrate at sputtering power of (a) 20 W; (b) 50 W; (c) 100 W; and (d) 200 W.

Figure 4.5. Plots of the thickness of Ag films according to the

substrate bias change while changing the working pressure at the sputtering power of (a) 20 W; (b) 50 W; (c) 100 W; and (d) 200 W.

Figure 4.6. Plots of the FWHM of Ag films of (111) peak according to the working pressure change while applying a bias to the substrate at sputtering power of (a) 20 W; (b) 50 W; (c) 100 W; and (d) 200 W.

Figure 4.7. Plots of the FWHM of Ag films of (111) peaks according to the substrate bias change while changing the working pressure at the sputtering power of (a) 20 W; (b) 50 W; (c) 100 W; and (d) 200 W.

Figure 4.8. Plots of the resistivity of Ag films according to the working pressure change while applying a bias to the substrate at sputtering power of (a) 20 W; (b) 50 W; (c) 100 W; and (d) 200 W.

Figure 4.9. Plots of the resistivity of Ag films according to the substrate bias change while changing the working pressure at the sputtering power of (a) 20 W; (b) 50 W; (c) 100 W; and (d) 200 W.

Figure 4.10. TEM images of Ag particles captured on an amorphous carbon membrane at the working pressure of (a) 2.5 mTorr; (b) 5 mTorr; (c) 10 mTorr; and (d) 20 mTorr at the sputtering power of 100 W and the substrate bias of 0 V.

List of Tables

Table 1.1. Summary of Si–H and Si–Si bond strengths in hydrogenated amorphous silicon.

Table 3.1 Deposition time for ~100nm film thickness for each sputtering power.

Table 3.2 The film growth rate for each sputtering power.

Table 3.3 Grain size of Ag films deposited on Si substrates for each sputtering power.

Table 3.4 The FWHMs of (111) peaks for each sputtering power.

Table 4.1. The ratio of the thickness change of Ag films when a bias is applied to the substrate at sputtering power of (a) 20 W; (b) 50 W; (c) 100 W; and (d) 200 W.

Table of Contents

Chapter 1. Introduction.....	1
1.1. Non–Classical Crystallization	1
1.2. Theory of Charged Nanoparticles (TCNs).....	2
1.3. Chemical Vapor Deposition (CVD)	5
1.4. Physical Vapor Deposition (PVD)	7
1.4.1. Evaporation.....	7
1.4.2. Direct Current (DC) Sputtering.....	8
1.5. Purpose of this study	11
 Chapter 2. The Effect of Charged Ag Nanoparticles on Thin Film Growth during DC Magnetron Sputtering	 15
2.1. Introduction	15
2.2. Experimental Methods.....	18
2.3. Results and Discussion.....	22
2.3.1. Capturing CNPs dDuring DC Sputtering with an Ag Target.....	 22

2.3.2. Ag Thin Film Deposition and Analysis	30
2.4 Conclusion	33
Chapter 3. Dependence of the Generation Behavior of Charged Nanoparticles and Ag Film Growth on Sputtering Power during DC Magnetron Sputtering	45
3.1. Introduction	45
3.2. Experimental Methods.....	48
3.3. Results and Discussion.....	51
3.4 Conclusion	61
Chapter 4. Effect of working pressure on the deposition behavior of Ag films during DC magnetron sputtering considering the generation of charged clusters	73
4.1. Introduction	73
4.2. Experimental Methods.....	76
4.3. Results and Discussion.....	79
4.4 Conclusion	88

Reference..... 100

Abstract in Korean 109

Chapter 1.

Introduction

1.1. Non–Classical Crystallization

The theory of classical crystallization was established based on believe that the building block of crystals should be individual ions, atoms or molecules. The theory of classical crystallization is described as a terrace–ledge–kink (TLK) model [1]. It is based upon the concept that the atomic potential energy on a crystal surface is determined by its bonding to neighboring atoms and that transitions simply involve the counting of broken and formed bonds. In this model, atoms or molecules are then absorbed on a terrace, diffused to a ledge and become incorporated in the crystal lattice at the kink.

However, thin film deposition behavior that is difficult to explain with the existing TLK model has been reported. A lot of research has been conducted to solve this puzzled phenomenon. Thanks to the

efforts of many researchers, it has been possible to successfully explain crystal growth that is difficult to understand with conventional theory. This new crystal growth mechanism is called non-classical crystallization[2–14].

The non-classical crystallization, which claims that crystal grow by the building block of nanoparticles, was not readily accepted in the early days. There are many reasons, but it can be summarized in two main ways. First, because the nanoparticles are very small, observation is very difficult. Second, it was difficult to be sure that the building blocks of crystal growth were nanoparticles. However, with the advancement of observation equipment, nanoparticles could be observed directly. For this reason, the non-classical crystallization was published as a related book and took a session at an international conference. Even now, many studies on non-classical crystallization are ongoing. Figure 1.1 shows a brief explanation of classical and non-classical crystallization.

1.2. Theory of Charged Nanoparticles (TCNs)

Hwang et al [8, 15–29] have done extensive study on non-

classical crystallization in the CVD process. they had published related books and more than 80 SCI papers. Studying non-classical crystallization, they proposed the theory of charged nanoparticles (TCNs). According to this theory, during CVD or some PVD processes, electrically charged nanoparticles are first produced in the gas phase, and these charged nanoparticles become a building block for crystal growth. Taking one step further from conventional non-classical crystallization, charge plays an important role in crystal growth. As shown in Figure 1.2, a diamond film grows on the insulate substrate such as a silicon, whereas a porous skeletal soot structure grows on an conducting substrate such as an iron under identical conditions in the diamond chemical vapor deposition (CVD) process using hot wires or plasma [16]. It was found that on an insulated substrate, charged nanoparticles (CNPs) maintained their charge. On the other hand, on a conductive substrate, charged nanoparticles lose their charge by tunneling and exist as neutral nanoparticles (NNPs). As a result, it was confirmed that the thin film deposition behavior was changed depending on the presence or absence of charge.

According to the TCN, if the nanoparticles are neutral, a porous

thin film tends to be formed by random Brownian coagulation, but if they are charged, a dense thin film tends to be formed in a highly orderly manner of deposition by self-assembly. Besides, when the particles become charged, the binding force between atoms weakens, so the particles have a high atomic mobility. As a result, CNPs undergo liquid-like coalescence when they land on the growing surface, and because of such liquid-like coalescence, even epitaxial films can be grown by CNPs.

Clare et al. [30] reported that the bond strength of Si-Si and Si-H is weakened by the presence of positive or negative charge in silane (SiH_4) and disilane (Si_2H_6) molecules by the ab-initio calculation. They calculated the difference in the energy to break a Si-H bond 19 in six species: SiH_3 , SiH_3^- , SiH_3^+ , SiH_4 , SiH_4^- , and SiH_4^+ . They also did similar calculations on Si-Si bond in the species: Si_2H_6 , Si_2H_6^- , Si_2H_6^+ , Si_2H_5 , Si_2H_5^- , and Si_2H_5^+ . The results of calculation are shown in Table 1.1. To summarize the results briefly, both the positive and negative charges lowered the bonding energy of Si-Si and Si-H. It can be explained that the charge weakens the binding energy of the nanoparticles and enhances the atomic diffusion. Therefore, the charged nanoparticles have liquid-like properties.

Due to this property, charged nanoparticles can make a dense thin film by self-assembly.

1.3. Chemical Vapor Deposition (CVD)

CVD technology is a method of forming a thin film on the surface of a substrate by supplying a gas containing a material of a thin film to be formed on a substrate and reacting chemically in the gas phase or the surface of the substrate. These chemical reactions include solid diffusion, hydrogen reduction, substitution reaction, and oxidation.

The main advantage of the CVD process lies in the fact that it utilizes many properties of the gas since the reactants used are gases. One consequence is that CVD, like most other plating/coating processes, is not a line of sight process and can be used to coat limited access surfaces. CVD offers many advantages over other deposition processes. These include a variety of coating materials based on metals, alloys and ceramics. Coatings can be deposited with very low porosity levels and high purity. This process can be economical in production and many parts are coated with many batch

numbers at the same time.

The CVD coating process typically uses temperatures in the range of 600 to 1100 °C. In these temperatures it can cause significant thermal effect on the substrate material. For example, steel is often heated to the austenitic phase region and after the coating process, appropriate heat treatment may be required to optimize the properties of the substrate.

Depending on the pressure at which the chemical reaction takes place, it can be classified as APCVD (Atmospheric Pressure CVD), LPCVD (Low Pressure CVD), and can be classified into PECVD (Plasma Enhanced CVD), HDPCVD (High Density Plasma CVD), and PACVD (Plasma Assisted CVD) by the method of enhancing the reaction of CVD, and it can be classified into MOCVD (Metal Organic CVD) by the classification of the applied precursor type.

In the semiconductor deposition process, the application range of CVD process technology is very wide. The CVD process introduced above can be said to be a core technology field applied to almost all processes, including insulation, gate wiring, capacitors, and metal

wiring in the entire semiconductor process field.

1.4. Physical Vapor Deposition (PVD)

Physical Vapor Deposition (PVD) is a variety of vacuum deposition methods that can be used to produce thin films and coatings. PVD is characterized by a process in which the material moves from the condensed phase to the vapor phase and then back to the thin film condensed phase. The most common PVD processes are sputtering and evaporation. PVD is used in the manufacture of items that require thin films for mechanical, optical, chemical or electronic functions.

1.4.1. Evaporation

Thermal Evaporation is one of the methods of Physical Vapor Deposition (PVD). In fact, the start of dry plating is thermal evaporation.

The deposition method of thermal evaporation is simple. In the chamber maintaining high vacuum, the material to be deposited is heated to a temperature sufficient to evaporate. The evaporated

material reaches onto the substrate placed on the top of the chamber and condenses, forming a thin film.

There are some things to consider here. First, the evaporation material goes straight. Therefore, if it collides with other gases or impurities in the middle, it loses its energy and may go to a place other than the substrate to be deposited. So, it requires the highest degree of vacuum compared to other PVDs.

Since the gases evaporated in thermal evaporation are only due to thermal energy, there is a disadvantage in that the energy may not be high enough and the adhesion may decrease. In addition, since the evaporation particles move in a linear motion, deposition is not performed on the corners or the back side of a three-dimensional specimen. For this, the substrate must be rotated or position of the evaporation source must be variously adjusted.

1.4.2. Direct Current (DC) Sputtering

One of the methods of Physical Vapor Deposition (PVD) Coating technique is Direct Current (DC) Sputtering. DC sputtering is mainly used for the deposition of metals and conductive materials. There are

two main advantages of DC sputtering. Firstly, it is easy to control the parameters used in the DC sputtering process, and secondly, it is possible to deposit a metal thin film very cheaply.

The basic configuration for DC sputtering only requires a target material directly connected to DC power and a substrate on which the thin film is to be deposited.

Since high vacuum is required for DC sputtering, the chamber is maintained at a very low pressure by a vacuum pump. After that, high purity inert gas is injected to adjust the working pressure. In general, argon gas is used a lot because it has good ability to efficiently transfer kinetic energy when colliding with high energy particles. Typical working pressures range from 0.5mTorr to 100mTorr.

In general, DC power in the range of -2 to -5 kV is applied to the target connected to the sputter gun which is the cathode which electrons source known as the negative bias. A positive charge is also applied to the substrate to be deposited which become the anode.

By this applied power, some of the ionized ions present in the

natural state are accelerated to the target. Argon ions that collide with the target get electrons from the target, which is an electron source, and return to the atom. This collision generates secondary electrons and moves away from the target by negative bias.

Electrically neutral argon atoms are ionized by inelastic collisions caused by secondary electrons emitted from the target, where the ionized positively charged argon ions are attracted back to the target.

By this continuous collision, argon is continuously ionized to maintain plasma. The ionized argon accelerated to the cathode sputters the target material. The sputtered particles reach the substrate to form a thin film.

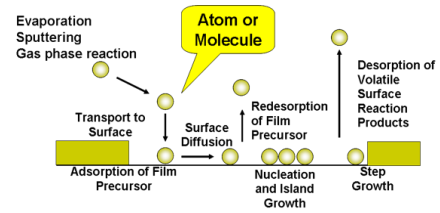
DC sputtering is an economical method of depositing in many types of a metal thin film, but due to the nature of a non-conductive material, there is a limitation in that the deposition is difficult due to the accumulation of electric charges over time.

1.5. Purpose of this study

The theory of charged nanoparticle has been studied a lot in CVD process. However, in the PVD process, research on this theory is insufficient. In this thesis, the theory of charged nanoparticles is extended from CVD to PVD to understand crystal growth. In particular, an experiment was conducted on charged nanoparticles for the first time in DC magnetron sputtering, which is the most widely used among PVDs. Through this study, the existence of charged nanoparticles during the DC magnetron sputtering process was confirmed, and their effect on the thin film growth was studied. As a result, we intend to understand more systematically DC magnetron sputtering and confirm that the charged nanoparticle theory can be applied to PVD as well.

Classical crystallization

“Building block : atom, ion, molecule”



Non-classical crystallization

“Building block : cluster, nanoparticles”

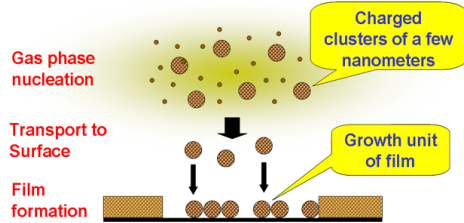


Figure 1.1. explanation of classical and non-classical crystallization.

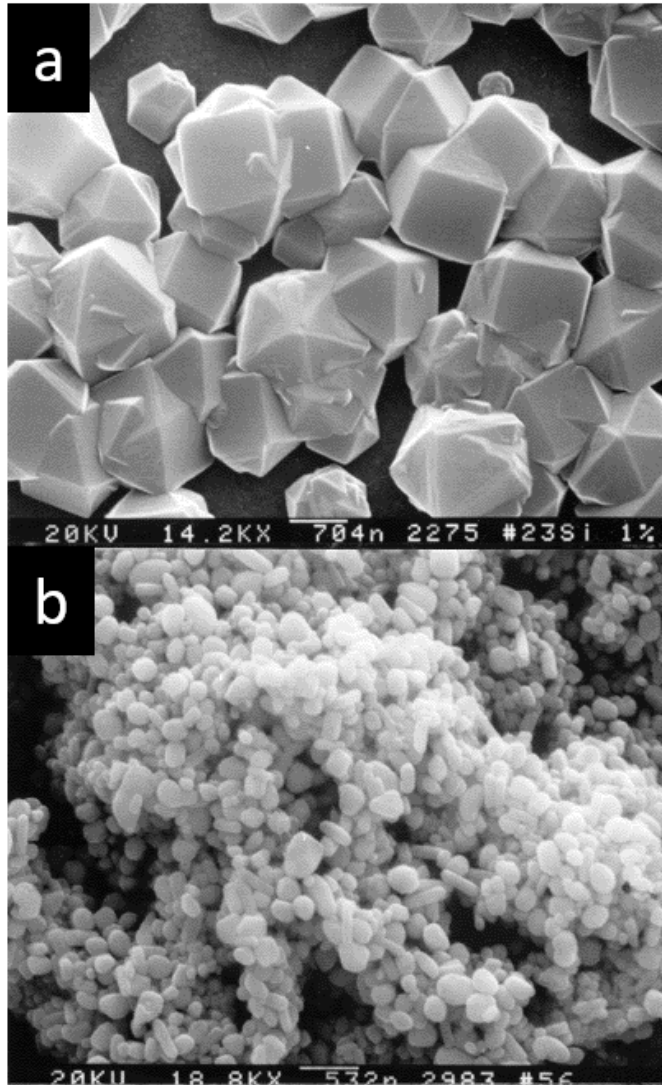


Figure 1.2. FESEM images of (a) cubic diamond deposited on the Si substrate and (b) carbon soot deposited on the Fe substrate [16].

COMPOUND	Si-H (eV)	Si-Si (eV)
SiH ₄ (optimized)	3.9	–
SiH ₄ ⁻ (optimized)	0.98	–
SiH ₄ ⁺ (optimized)	0.30	–
SiH ₄ ⁻ (unoptimized)	1.35	–
SiH ₄ ⁺ (unoptimized)	0.09	–
Si ₂ H ₆ (optimized)	3.5	3.2
Si ₂ H ₆ ⁻ (optimized)	1.02	1.11
Si ₂ H ₆ ⁺ (optimized)	1.59	1.6
Si ₂ H ₆ ⁻ (unoptimized)	1.34	1.3
Si ₂ H ₆ ⁺ (unoptimized)	1.49	1.6

Table 1.1. Summary of Si-H and Si-Si bond strengths in hydrogenated amorphous silicon[30].

Chapter 2.

The Effect of Charged Ag Nanoparticles on Thin Film Growth during DC Magnetron Sputtering

2.1. Introduction

Ag thin films and nanoparticles are used in optical applications [31–35], microelectronics [36, 37] and biomedical applications [38–40] because of their excellent electrical and optical properties, good chemical and thermal stability and antibacterial effects. Ag thin films and nanoparticles are made in various ways, such as thermal evaporation [33, 41], direct current (DC) sputtering [42, 43], radio frequency (RF) sputtering [44–46] and high power impulse magnetron sputtering (HiPIMS) [47, 48].

In general, the thin film deposition mechanism is described as a

terrace–ledge–kink (TLK) model [1], where an adatom moves around on the terrace until it finds a kink at the ledge; it is then incorporated into a crystal. In this model, the building block is an individual atom, molecule or ion. This way of crystal growth is called classical crystallization. However, some deposition behavior of thin films that is difficult to explain by the conventional TLK model has been observed. Such deposition behavior could be successfully explained by the new film growth mechanism, where the building block is nanoparticles generated in the gas phase. This new mechanism is called non–classical crystallization [6, 8, 10, 14, 49–51].

Hwang et al. [8] extensively studied the thin film growth by non–classical crystallization in a chemical vapor deposition (CVD) process. They suggested that during the CVD process, electrically charged nanoparticles (CNPs) are formed in the gas phase, and these CNPs can be a major deposition flux of thin films. In this case, the deposition unit of thin films is neither an atom nor molecule but a nanoparticle. Additionally, here, an electric charge carried by nanoparticles plays an important role in the evolution of dense films by non–classical crystallization. They called this new thin film growth mechanism “the theory of charged nanoparticles (TCN)” .

According to the TCN, if the nanoparticles are neutral, a porous thin film tends to be formed by random Brownian coagulation, but if they are charged, a dense thin film tends to be formed in a highly orderly manner of deposition by self-assembly. Besides, when the particles become charged, the binding force between atoms weakens, so the particles have a high atomic mobility. As a result, CNPs undergo liquid-like coalescence when they land on the growing surface, and because of such liquid-like coalescence, even epitaxial films can be grown by CNPs. For example, a fully epitaxial silicon film could be grown on a silicon wafer at 550 ° C under the bias of -1000 V during radio frequency plasma-enhanced chemical vapor deposition (RF-PECVD) [52].

In relation to the weakening of the binding force between atoms in CNPs, Clare et al. [30] reported by ab initio calculations that the bond strengths of Si-Si and Si-H are weakened by the presence of positive or negative charges in silane (SiH_4) and disilane (Si_2H_6) molecules.

Although the film growth by CNPs has been studied extensively in CVD, not much work has been done in physical vapor deposition

(PVD). Jeon et al. [41] confirmed the generation of charged Ag nanoparticles during thermal evaporation by current measurements combined with the bias experiment. Kwon et al. [53] confirmed the generation of charged Ti nanoparticles and their contribution to film growth during RF magnetron sputtering. This means that it is highly probable that CNPs would also be generated in the DC magnetron sputtering.

The purpose of this study was to confirm the generation of CNPs and their contribution to film growth during DC magnetron sputtering of Ag. For this, we tried to capture nanoparticles on a membrane for transmission electron microscopy (TEM) and to deposit films under the bias applied to the substrate holder.

2.2. Experimental methods

Figure 2.1 (a) shows a schematic of the DC magnetron sputtering system. An Ag target 7.62 cm in diameter was used. The distance between the Ag target and substrate was 24 cm. The reason why this distance was made larger than that typically used in sputtering was to examine the effect of the electric bias applied to the substrate

holder. An ultrathin amorphous carbon TEM membrane (Ted Pella, Inc., Redding, CA, USA) for capturing sputtered particles was placed on a substrate holder, which was electrically insulated from the grounded sputter system in order to apply the electric bias. By particle capturing, we mean the deposition of the sputtering flux on the TEM membrane for a short exposure time, usually less than 10 s. A p-type Si (100) substrate was used for film deposition. The Cu mesh, which was grounded, was installed above the substrate holder to minimize the effect of the substrate bias on the plasma. The hole size of the grounded mesh was 150 μm , which was determined not to exceed the Debye length of the plasma [54].

A shutter was placed above the grounded mesh to control the particle capturing or film deposition. By opening or closing the shutter, the time for capturing and deposition could be controlled. The current of the substrate holder was measured during the sputtering process in order to check whether any of the sputtering flux was charged. The current was measured by a pico-ammeter (KEITHLEY 6487, Tektronix, Cleveland, OH, USA). Figure 2.1(b) shows the current measured on the substrate holder during the time interval when the plasma for sputtering was turned on and off. Note that no bias was

applied to the substrate holder. Definitely, an appreciable amount of negative current was measured as soon as the plasma was turned on. Most of the flux carrying a negative charge would be electrons. However, we cannot rule out the possibility that some of the sputtered flux might carry the negative charge. This possibility can be confirmed by the bias experiment.

DC plasma power, Ar gas pressure and substrate temperature were 200 W, 1.33 Pa (10 mTorr) and room temperature, respectively, for all experiments. To confirm that the charged flux contributes to the deposition, the capturing and deposition behavior were compared for the samples prepared under the biases of +300, 0, and -300 V applied to the substrate holder.

The bias applied to the substrate affects the plasma. To eliminate this effect, a grounded mesh was installed between the plasma and the substrate. As the bias applied to the substrate increases, the Debye length of the plasma decreases. In order for the bias not to affect the plasma, the hole size of a grounded mesh should be smaller than the Debye length. If the hole size is too small, the sputtered flux coming to the substrate would become very small and the experiment

would not be appropriate. If the bias is too small, the substrate bias becomes smaller than the kinetic energy of the sputtered particles, so the bias would not have any effect. Considering these two factors, the biases of ± 300 V were chosen.

To see the time evolution of particles, the capturing experiments were performed for 1, 3, 5, 7 and 10 s under all bias conditions. Additionally, in order to study the effects of the charged flux on the film properties, the thin film was deposited for 30 min under the three bias conditions mentioned above.

The Ag particles captured on the amorphous carbon membrane were observed by TEM (FEI, Tecnai F20, Hillsboro, OR, USA). The open source software ImageJ (1.51k, National Institutes of Health, Bethesda, MD, USA) was used to analyze the TEM images. ImageJ analyzed the images in pixels. It calculated the particle size, the nanoparticle density and the total area by setting the appropriate threshold value. The microstructure of the Ag films was investigated by field-emission scanning electron microscopy (FESEM, Carl Zeiss, SUPRA, Oberkochen, Germany). TEM and FESEM were operated at accelerating voltages of 200 and 2 kV, respectively. The crystallinity

of the films was analyzed by X-ray diffraction (XRD, PANalytical, X'pert-Pro, Almelo, The Netherlands) at a 2θ scanning range of $30^\circ \sim 80^\circ$ with the Cu K_α ($\lambda = 1.5418 \text{ \AA}$) source. The resistivity of Ag films was measured using a four-point probe (CMT-SR2000N, Materials Development Corporation, Founex, Switzerland).

2.3. Results and Discussion

2.3.1 Capturing CNPs During DC Sputtering with an Ag Target

Figure 2.2 shows the time evolution of TEM images of sputtered Ag particles captured on the ultrathin amorphous carbon membrane under the substrate bias of 0 V or in the absence of the bias. Ag particles captured for 1, 3, 5, 7, and 10 s had the average diameters of 1.7 ± 0.06 , 2.0 ± 0.05 , 2.2 ± 0.14 , 2.6 ± 0.09 and 3.1 ± 0.08 nm; and the nanoparticle densities of 18415 ± 421 , 24068 ± 418 , 28281 ± 930 , 28606 ± 531 and 22736 ± 269 per μm^2 , respectively. Those data were estimated using an image analysis tool of ImageJ (1.51k) [55]. The size of Ag particles continued to increase with the capture time. However, the number density increased up to 7 s and then decreased at 10 s.

Most of Ag particles captured for 1 s in Figure 2.2(a) were not

crystalline but amorphous. This aspect was revealed by the high resolution TEM (HRTEM) image and the fast Fourier–transform (FFT) inset in Figure 2.3(a). As the size of Ag particles increases, they tend to be crystalline. This transition from amorphous to crystalline phase occurred at ~ 2.5 nm, where roughly 50% of them were amorphous and the other 50 % were crystalline. Most of Ag particles captured for 10 s in Figure 2.2(e), which had the average size of ~ 3.1 nm, were crystalline, as revealed by the high resolution TEM image and the FFT inset in Figure 3b.

Figure 2.4 shows the time evolution of TEM images of the sputtered Ag particles captured on the amorphous carbon membrane under the substrate bias of +300 V. Ag particles captured for 1, 3, 5, 7 and 10 s had the average diameters of 1.7 ± 0.12 , 2.0 ± 0.1 , 2.3 ± 0.09 , 3.0 ± 0.22 and 3.4 ± 0.14 nm; and the nanoparticle densities of 18911 ± 731 , 31549 ± 1076 , 30635 ± 647 , 23681 ± 585 and 20289 ± 487 per μm^2 , respectively. Although the average size of Ag particles continued to increase with the capture time, the number density increased up to 3 s and then decreased up to 10 s.

Figure 2.5 shows the time evolution of TEM images of the

sputtered Ag particles captured under the substrate bias of -300 V. Ag particles captured for 1, 3, 5, 7 and 10 s had the average diameters of 1.6 ± 0.12 , 1.8 ± 0.24 , 2.0 ± 0.14 , 2.5 ± 0.09 and 3.0 ± 0.1 nm and the nanoparticle densities of 15317 ± 454 , 21497 ± 1531 , 25230 ± 1050 , 18415 ± 418 and 17919 ± 254 per μm^2 , respectively. The average size of Ag particles continued to increase with the capture time, but the number density increased up to 5 s then decreased up to 10 s.

In order to compare the time evolution of Ag particles captured up to 10 s under the three bias conditions of 0, +300 and -300 V, their average diameter, number density and total area are plotted against the capture time, respectively, in Figure 2.6(a) - (c).

Figure 2.6(a) shows that the average diameter of particles captured under +300 V was larger than those captured under 0 and -300 V. Additionally, the size distribution of Ag nanoparticles under each capture condition can be seen in Figure 2.11. Figure 2.6(b) shows that the number density of Ag particles increased up to a certain capture time and then decreased in all three bias conditions. Considering the relatively high fraction of the unoccupied area on the

carbon membrane shown in Figures 2.2, 2.4 and 2.5, the number density of Ag particles was expected to increase continuously with increasing capture time. This unexpected behavior is discussed later.

Figure 2.6(c) shows that the total area of Ag particles on the carbon membrane increased with increasing capture time in all three bias conditions. The total area was largest for +300 V and smallest for -300 V. Since the total area represents the total flux coming from sputtering, it indicates the deposition flux. The difference in the deposition flux under the different bias condition indicates that some of the flux was electrically charged. Considering that the deposition flux became maximum for +300 V, medium for 0 V and minimum for -300 V, an appreciable amount of the flux must have been negatively charged. The positive flux, if any, seemed to be minor or negligible, and the neutral flux seemed to be major. To determine the fraction of the negative flux, the thicknesses of films, which were deposited under the three bias conditions, should be compared. This result will be explained later.

Then, why are small particles in Figures 2.2(a) and 2.3(a) amorphous? Additionally, why are large particles in Figures 2.2(e)

and 2.3(b) crystalline? When combining the results of Figure 2.2(a) and (e) and Figure 2.3(a) and (b), it can be said that the Ag particles or films are amorphous in the initial stage of deposition but become crystalline in the later stage. Then, how can such a transition occur at room temperature?

One possible explanation is based on the presence of charge on the growing surface, which is clearly revealed in the current measurement in Figure 2.1(b). According to the phenomenon of melting point depression of small particles [56, 57], the melting point of ~ 1.7 nm Ag particles would decrease far lower than that of the bulk Ag. However, the melting point cannot decrease down to room temperature. Observing and analyzing the behavior of charged nanoparticles, Hwang [8] suggested a hypothesis that the presence of charge would decrease the bond strength of small nanoparticles and can make them liquid-like.

Based on the hypothesis that small charged nanoparticles have liquid-like behavior, it can be explained why Ag particles of ~ 1.7 nm in Figures 2.2(a) and 2.3(a) have an amorphous phase on the amorphous carbon membrane. Considering the appreciable amount of

negative current measured during sputtering in Figure 2.1(b), Ag particles of ~ 1.7 nm in Figures 2.2(a) and 2.3(a) were expected to be negatively charged. Since negatively charged Ag particles of ~ 1.7 nm would be liquid-like, they would accommodate the structure of the substrate. If the substrate is crystalline, it tends to have a crystalline structure, and if the substrate is amorphous, it tends to have an amorphous structure. In other words, if charged nanoparticles are small enough to have liquid-like behavior, they tend to have the structural similarity with the substrate to decrease the interfacial free energy. Even if small Ag particles have a crystalline structure in the gas phase, they tend to follow the structure of the substrate. Since the amorphous carbon membrane was used as a substrate for what is shown in Figure 2.3(a), charged Ag particles of ~ 1.7 nm would have the amorphous structure.

As the size of Ag particles increases, however, the bulk free energy term would become dominant over the interfacial free energy term and then the crystalline phase would become more stable. In this case, the large crystalline Ag particles would remain crystalline even if they landed on the amorphous substrate.

Then, why does the number density decrease with the capture

time in Figure 2.6(b)? The decrease of the number density occurred in the earliest time of 3 s for Ag particles captured under the bias of +300 V. That leads to another question as to why the bias of +300 V causes the decrease of the number density in the earliest time. These two questions could be approached from the effect of charge.

Considering the negative current data in Figure 2.1(b), an appreciable amount of the negative flux including electrons would exist in the sputtering chamber. The largest total area of Ag particles in Figure 2.6(c) for the bias of +300 V indicates that the bias of +300 V attracts the negatively charged flux. As a result, the largest number of negative charges would build up on the Ag particles for the bias of +300 V. The decrease of the number density in Figure 2.6(b) indicates that the Ag particles undergo coalescence accompanied by the movement of the center of the particle mass. For such movement, a force between Ag particles should exist. The electrostatic interaction between the charged spherical conducting particles of the same sign can be attractive when their size difference is large enough, considering the following equation [58].

$$F = \frac{q_1 q_2}{4\pi\epsilon_0 d^2} - \frac{q_2^2 r_1 d}{4\pi\epsilon_0 (d^2 - r_1^2)^2} - \frac{q_1^2 r_2 d}{4\pi\epsilon_0 (d^2 - r_2^2)^2} + \dots, \quad (2.1)$$

where the sphere of radius r_1 has a net charge q_1 and the other of radius r_2 has charge q_2 ; d is the distance between the particle centers and $1/4\pi\epsilon_0$ the permittivity. The first term is the well-known Coulomb equation, which can be attractive or repulsive depending on the signs of the two interacting particles. The second and third terms come from the image force, which are attractive regardless of the sign of the charge. From the fourth term, it is the corresponding to the second image force by the first image force from the second and third terms. Actually, these values are very small and negligible. This equation reveals that if a large spherical particle has a large number of charges, it will attract a small charged particle of the same sign.

The decrease of the number density occurs after 3, 5 and 7 s, respectively, for the biases of +300, -300 and 0 V. Therefore, it seems that the magnitude of the attractive Coulomb interaction between charged Ag particles of the same sign described by Equation (2.1) would be in the order of +300; -300 and 0 V. We do not clearly understand why the bias of -300 V has a stronger effect than that of 0 V. One possibility could be that the bias of -300 V builds up an appreciable number of positive charges on Ag particles.

2.3.2 Ag Thin Film Deposition and Analysis

In order to examine the effect of the negatively charged particles on the thin film growth, Ag thin films were deposited for 30 min under the conditions where biases of +300, 0, and -300 V were applied to the substrate holder. Figure 2.7 shows cross-section FESEM images of the Ag films deposited on a Si substrate. Thicknesses of the Ag thin films, determined by the cross-section FESEM images, were 68.9, 77.6 and 85.0 nm, respectively, for the biases of -300, 0 and +300 V. Compared to the thickness of the film deposited under 0 V, the thickness of the film deposited under +300 V increased by 9.5 % and the thickness under -300 V decreased by 11.2 %. The decrease of the film thickness under -300 V would have come from repelling negatively-charged particles. The increase of the film thickness under +300 V would have come from attracting negatively-charged particles. Such a bias effect on the film thickness indicates that roughly 10 % of the flux was negatively charged and the amount of positively charged flux was negligible.

In order to examine how the deposition of the negatively-charged flux affects the film quality, the surface morphology of films was observed by FESEM and the crystallinity of films was analyzed

by XRD. Figure 8 shows top-view FESEM images of Ag films deposited on a Si substrate. The grain size of the thin film deposited under +300 V (Figure 2.8(c) and (f)) was larger than that deposited under 0 V (Figure 2.8(b) and (e)) and that deposited under -300 V (Figure 2.8(a) and (d)). The grain size became larger under the condition of high atomic mobility, which would be favored by the highest charge density condition of Ag particles deposited under the bias of +300 V (Figure 2.8(c) and(f)). The difference in the grain size among Figure 2.8(a)~(c) can also be explained by the charge effect.

Figure 2.8(a) and (d) shows some pores among grains in comparison with Figure 2.8(b) and (d) Figure 2.8(c) and (f), where pores were hardly found. Such pore formation in Figure 2.8(a) and (d) seems to be related to the repulsion of negatively-charged Ag particles by the bias of -300 V. Therefore, the pore formation is attributed to the lack of charged Ag particles, which have a liquid-like property or high atomic mobility. The lack of negatively-charged Ag particles might also be related with the small grain size in Figure 2.8(a) and (d).

The large grain size would result in the high crystallinity. In relation to this, XRD spectra of the films deposited under -300, 0 and +300 V are compared in Figure 2.9. The peaks at $2\theta = 38.11^\circ$ and 44.27° indicate (111) and (200) orientations of Ag, respectively. When +300 V was applied, both peaks of (111) and (200) showed the highest intensity. On the other hand, when -300 V was applied, both peaks of (111) and (200) showed the lowest intensity. The crystallinity of the Ag thin films can be compared using a full width at half maximum intensity (FWHM) of the (111) peak. The FWHM is inversely proportional to the grain size according to the Scherrer equation,

$$\tau = \frac{K\lambda}{\beta \cos\theta} \quad (2.2)$$

where τ is the mean size of the grain, K is a dimensionless shape factor, λ is the X-ray wavelength of Cu $K_{\alpha 1}$, β is the FWHM and θ is the Bragg angle, so the smaller the FWHM, the better the crystallinity [59]. The film had the lowest FWHM value of 0.44 when the substrate bias was +300 V, and the highest value of 0.53 when the substrate bias was -300 V. It means that for +300 V, the film had the largest grain, which agrees with the result in Figure 2.8. Therefore, it can be said that the Ag film of the best crystallinity

among the three bias conditions was obtained when +300 V is applied.

The resistivity was measured to evaluate the Ag thin film quality. Figure 2.10 shows the resistivity of each Ag thin film deposited under each bias condition. The theoretical resistivity of Ag was $1.59 \mu\Omega \cdot \text{cm}$ (at 20°C). The resistivities of the Ag thin films with +300 and -300 V applied to the substrate holder were, respectively, smallest with $3.67 \mu\Omega \cdot \text{cm}$ and highest with $8.87 \mu\Omega \cdot \text{cm}$. As in the results of Figures 8 and 9, the Ag thin film with +300 V applied to the substrate showed the best film quality.

2.4. Conclusion

The generation of charged Ag particles and their contributions to film growth were confirmed through the bias experiment and the current measurement during the DC magnetron sputtering. Roughly 10 % of sputtered Ag particles were negatively charged and the positive bias applied to the substrate holder increased the film growth rate and produced a film of better crystallinity than that produced by the negative bias. Based on these results, we suggest that the bias can be a new process parameter in sputtering.

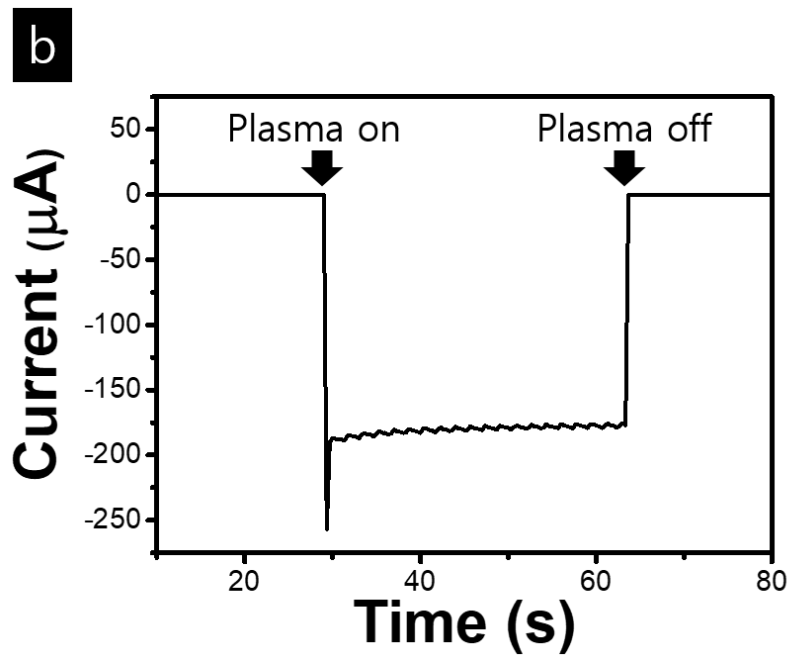
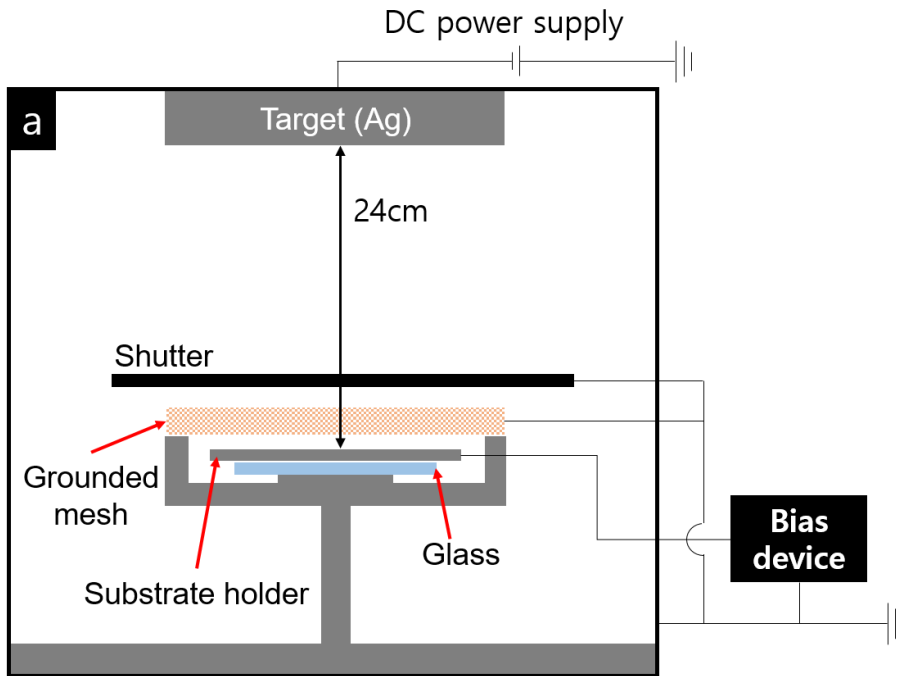


Figure. 2.1. (a) Schematic of the DC sputtering system and (b) the current measured on the substrate holder.

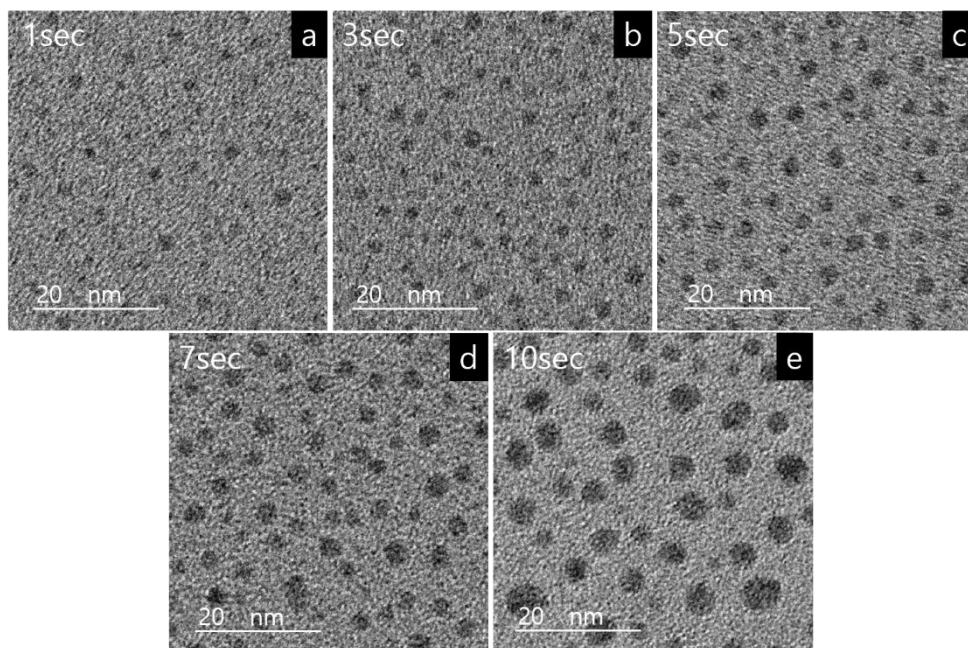


Figure 2.2. TEM images of Ag particles captured on an amorphous carbon membrane at the substrate bias of 0 V for (a) 1 s, (b) 3 s, (c) 5 s, (d) 7 s and (e) 10 s.

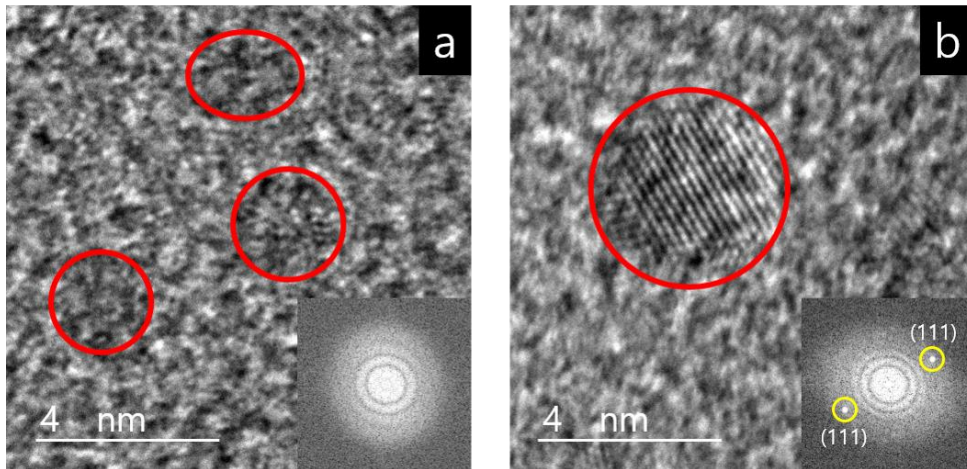


Figure 2.3. HRTEM image and FFT information (inset of the lower right in the image) of Ag sputtered particles captured on an amorphous carbon membrane at the substrate bias of 0 V for (a) 1 s and (b) 10 s.

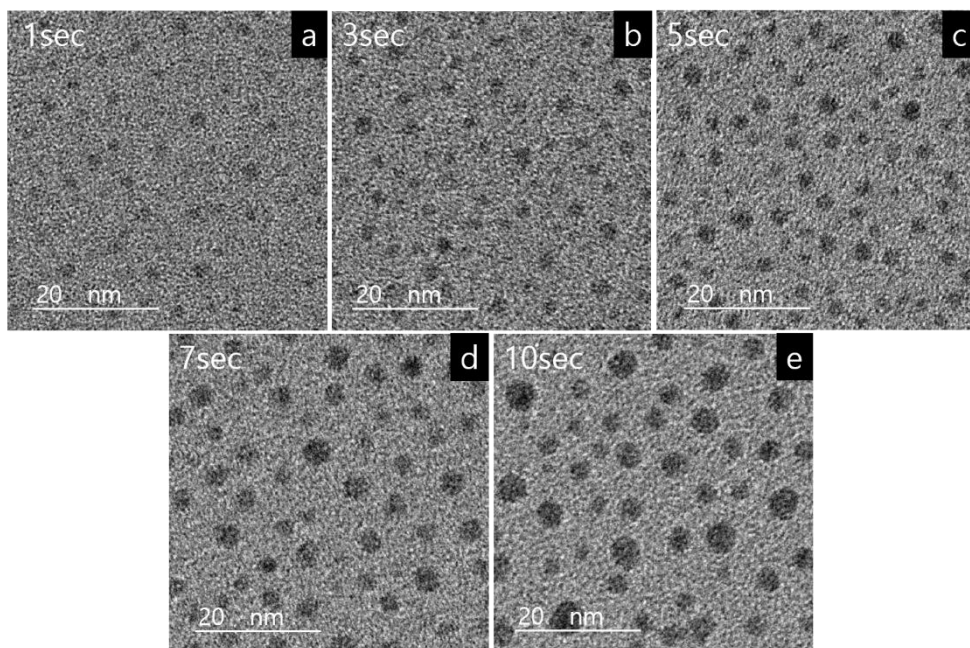


Figure 2.4. TEM images of Ag particles captured on an amorphous carbon membrane at the substrate bias of +300 V for (a) 1 s; (b) 3 s; (c) 5 s; (d) 7 s; and (e) 10 s.

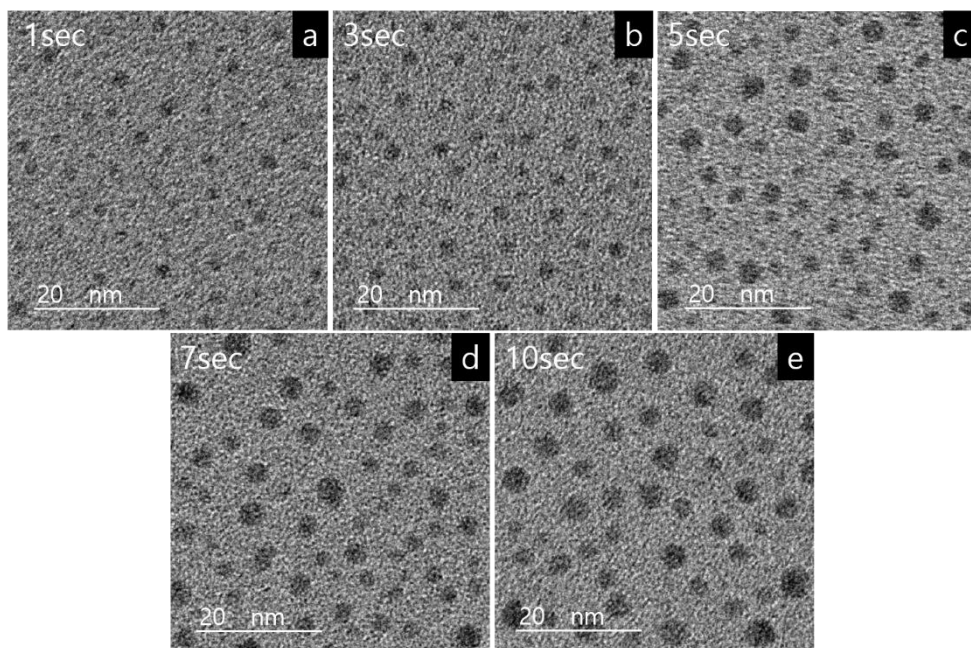


Figure 2.5. TEM images of Ag particles captured on an amorphous carbon membrane at the substrate bias of -300 V for (a) 1 s; (b) 3 s; (c) 5 s; (d) 7 s; and (e) 10 s.

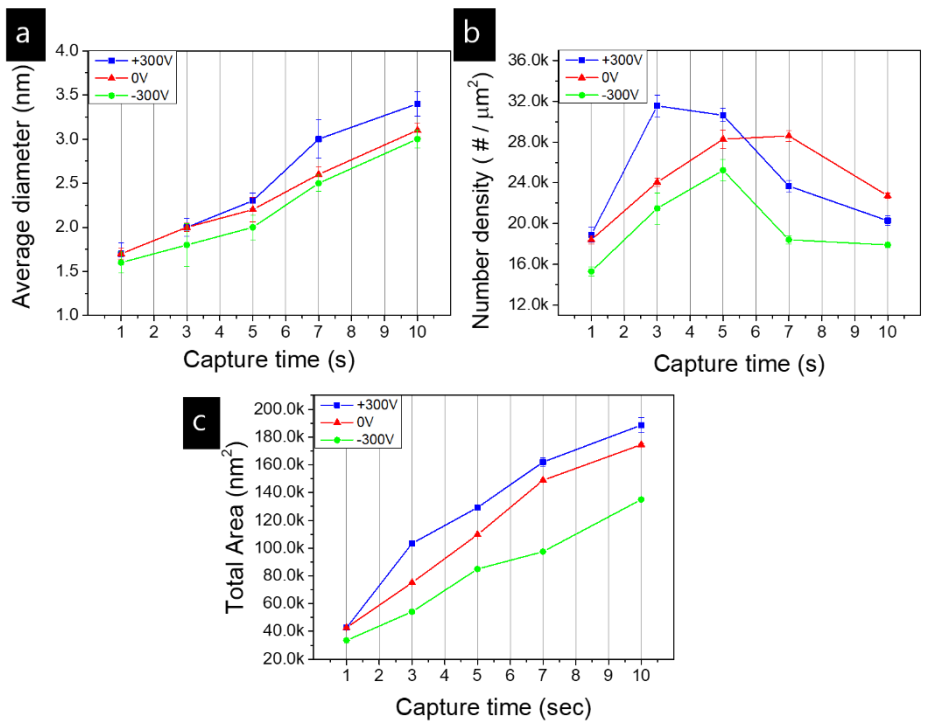


Figure 2.6. Plots of (a) particle average diameter; (b) particle count per μm^2 ; and (c) total area of Ag particle per μm^2 against the capture time analyzed by the ImageJ program.

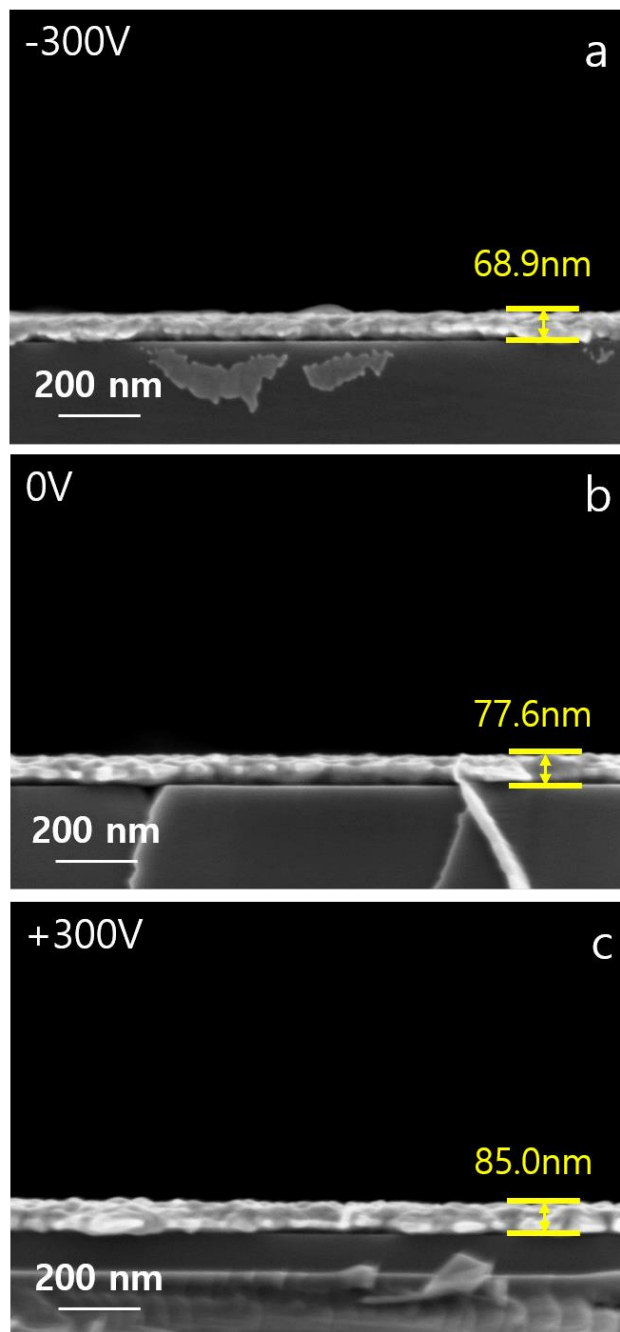


Figure 2.7. Cross-section FESEM images of the Ag films deposited on Si substrates at the electric biases of (a) -300 V; (b) 0 V; and (c) +300 V.

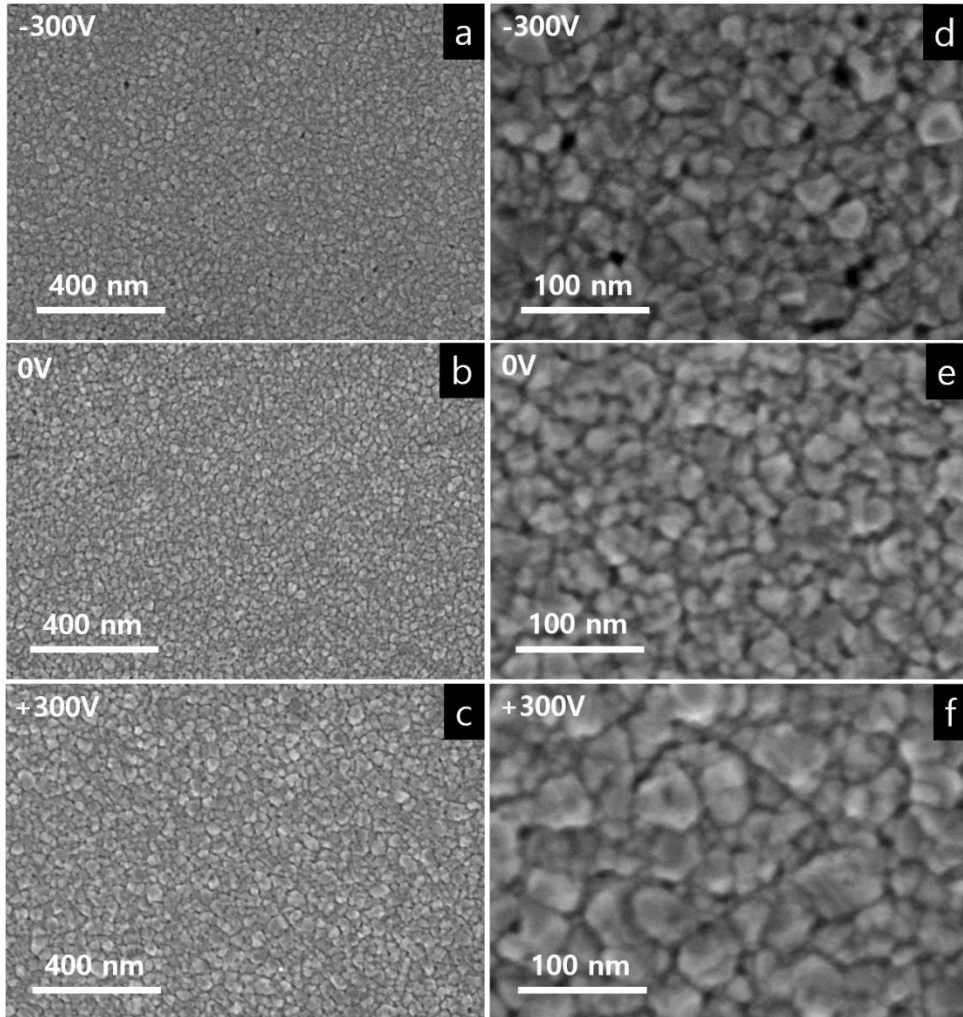


Figure 2.8. Top-view FESEM images of ((a)~(c)) low magnification and ((d)~(f)) high magnification of the Ag films deposited on Si substrates at the electric biases of ((a) and (d)) -300 V ((b) and (e)) 0 V and ((c) and (f)) +300 V.

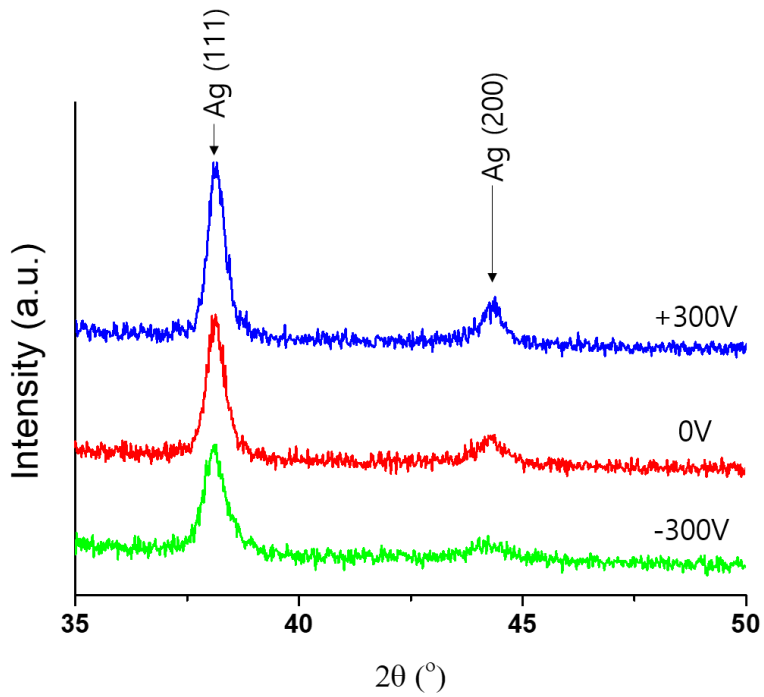


Figure 2.9. XRD data of the Ag films deposited at the electric biases of -300, 0 and +300 V in the 2θ range of 35° - 50° . The FWHMs of (111) peaks for -300, 0 and +300 V are 0.53, 0.47 and 0.44, respectively.

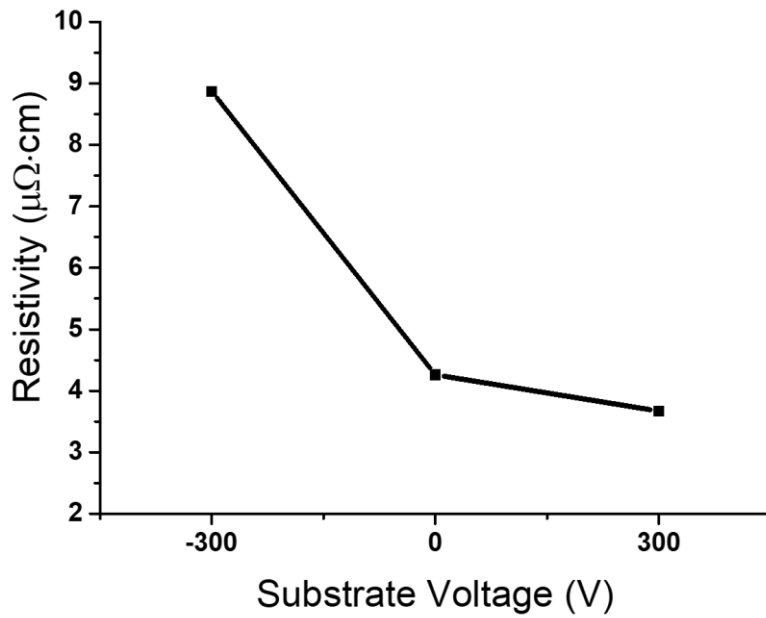


Figure 2.10. Resistivity of the Ag films deposited at the electric biases of -300, 0 and +300 V.

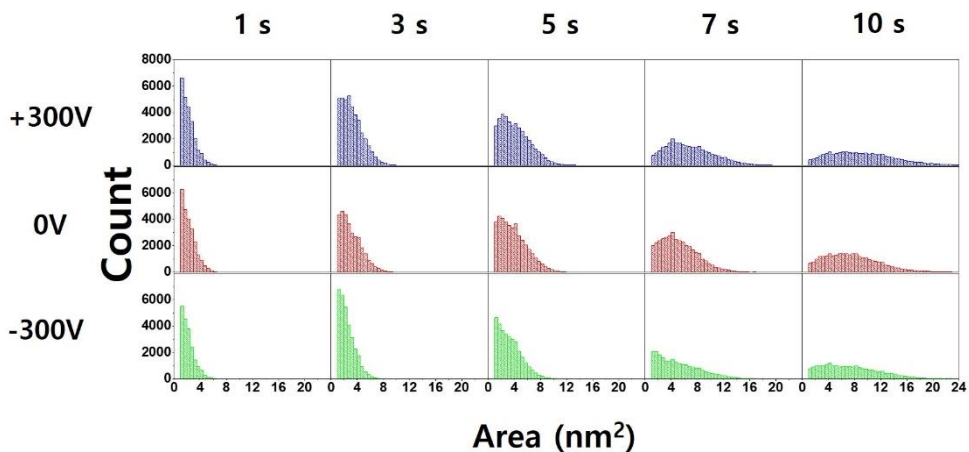


Figure 2.11. Gaussian graph for Ag nanoparticles size distribution under each capture condition.

Chapter 3.

Dependence of the Generation Behavior of Charged Nanoparticles and Ag Film Growth on Sputtering Power during DC Magnetron Sputtering

3.1. Introduction

In general, crystal growth can be described using a terrace–ledge–kink (TLK) model [1], where the building block is an atom, ion or molecule. However, several phenomena are difficult to explain using the TLK model, but can be explained by the so–called non–classical crystallization mechanism, where the building block is nanoparticles [6–8, 10–14, 50, 51, 60–64].

Hwang et al. [8] reported that, for thin film growth by chemical

vapor deposition (CVD), most films and nanostructures are grown using charged nanoparticles (CNPs) as building blocks. It was reported that the charge plays a very important role in the evolution of dense films and nanostructures: neutral nanoparticles produce a porous structure, whereas CNPs produce a dense structure. For example, Yoon et al. [65] compared the deposition behavior of charged silicon nanoparticles between electrically floating and grounded silicon substrates, and observed that silicon nanowires or dense films were grown on the floating substrate, whereas a porous structure was grown on the grounded substrate.

Park et al. [66] compared the plasma dewetting kinetics of Sn films, deposited by sputtering on a native oxide of silicon, between floating and grounded conditions of the surface, and observed that the plasma dewetting kinetics were much faster in the floating condition than in the grounded one. Based on such deposition behavior of CNPs, they suggested that charge enhances the atomic mobility of nanoparticles or renders them liquid-like. By exploiting the liquid-like property of CNPs, Park et al. [52] deposited a fully epitaxial silicon film on a silicon wafer at 550 ° C under a substrate bias of $-1,000$ V using radio frequency plasma-enhanced chemical

vapor deposition (RF-PECVD).

Although film growth by CNPs has been studied extensively in CVD, there have been fewer reports on film growth by CNPs using physical vapor deposition (PVD) methods, such as sputtering. Yoshida et al. [67, 68] reported the concept of film growth by ‘hot cluster epitaxy’ or ‘plasma flash evaporation’, where nanoparticles were evaporated by thermal plasma and the condensed clusters contributed to film growth. Although they did not mention the role of charge, we believe that their clusters were charged. Kwon et al. [53] confirmed the generation of Ti CNPs, and their contribution to film deposition during RF magnetron sputtering. Jang et al. [69] also confirmed the generation of negatively charged Ag nanoparticles, and their contribution to film deposition during DC magnetron sputtering.

This study is an extension of this previous work [69], focusing on the effect of sputtering power on the deposition behavior of films during DC magnetron sputtering. The key finding of this study is that most of the sputtered flux is in the form of individual atoms under a low sputtering power of 10 W, while neutral clusters are generated

when the sputtering power is 20~50 W, and charged clusters when the sputtering power is 100~300 W.

3.2. Experimental methods

Ag thin films were deposited on a p-type Si (100) substrate by DC magnetron sputtering. The silicon substrate was blown with air to remove dust. After that, it was immersed in an ethanol solution and ultra-sonication was conducted for 10 min to remove contaminants. Figure 3.1 shows DC magnetron sputtering chamber. An Ag target 7.62 cm in diameter (99.999 % purity) was used. The Ag target was connected to a DC power supply (psplasma, Inc., SDC1022A, Hwaseong, South Korea), and the distance between the target and substrate was fixed at 24 cm. The substrate was placed in an electrically floating holder to apply the electrical bias. A grounded Cu mesh was installed on the substrate holder so that the bias would not affect the plasma. The hole size of the grounded mesh was shorter than the Debye length of the plasma, to prevent the plasma from affecting the substrate, and the area of each square hole was 150 μm x 150 μm . The deposition of Ag films was started by opening, and terminated by closing, the shutter, which was installed above the

grounded mesh.

The base pressure of the chamber was $\sim 3 \times 10^{-6}$ mTorr, and the working pressure was maintained at 10 mTorr using Ar gas. The substrate at room temperature was slightly heated during sputtering, however, the temperature, measured by a thermocouple placed near the substrate, did not exceed 120°C even at the highest sputtering power of 300 W. To study the effect of sputtering power on the deposition behavior of Ag films, DC sputtering powers of 10, 20, 50, 100, 200 and 300 W were applied. Since the thin film deposited at the sputtering power of 10W has a very low deposition rate, it was difficult to analyze the resistivity by a four-point probe and the crystallinity by XRD if the deposition time is the same as that of the other sputtering power. Because of this problem, we tried to fix the film thickness to 100 nm. To achieve this, Table 3.1 shows deposition times for each sputtering power.

In addition, to determine whether charged particles contribute to film deposition during sputtering, biases of -300, 0 and +300 V were applied to the substrate holder at plasma powers of 10 and 200 W.

Deposition times of 420 and 20 min were used for the plasma powers of 10 and 200 W, respectively, to produce films of similar thickness.

The surface and cross-section of the Ag films were observed by field-emission scanning electron microscopy (FESEM; SUPRA; Carl Zeiss, Oberkochen, Germany). The FESEM measurements were conducted at an accelerating voltage of 2 kV. A focused ion beam (FIB; SMI3050SE; Seiko Instruments, Chiba, Japan) was used to prepare the sample for observation by transmission electron microscopy (TEM; Tecnai F20; FEI, Hillsboro, OR, USA). The TEM measurements were conducted at an accelerating voltage of 200 kV. To examine the crystallinity, the deposited Ag films were analyzed by XRD (PANalytical, X' Pert-Pro, Almelo, The Netherlands) at a 2θ scanning range of $30^\circ \sim 80^\circ$ with a Cu K_α ($\lambda = 1.5418 \text{ \AA}$) source. To evaluate the electrical property of the film, the resistivity was measured using a four-point probe (CMT-SR2000N; Materials Development Corporation, Founex, Switzerland).

3.3 Results and Discussion

Figure 3.2 shows cross-sectional FESEM images of the Ag films deposited on the Si substrates at different sputtering powers. Depending on the sputtering power, it took 25 ~ 700 min to deposit Ag films of ~100 nm. The average value of the film thickness was obtained by measuring 10 locations of the cross section using FESEM. The average value was presented with an error range of 95 % confidence. The film growth rate was determined by dividing the measured film thickness by the deposition time. The dependence of the film growth rate on the sputtering power is shown in Table 3.2.

The film growth rate increased with increasing sputtering power up to 200 W, although not linearly, and then decreased at 300 W. The reason for the decreasing film growth rate at a sputtering power of 300 W is re-sputtering caused by the high-energy sputtered flux [70].

Figure 3.3 shows top-view FESEM images of the surface morphology of the Ag films deposited on Si substrates for different

sputtering powers. The grain size for each sputtering power is shown in Table 3.3.

The grain size was largest at the sputtering power of 10 W, and tended to decrease with increasing sputtering power. In general, the grain size of thin films is known to be proportional to the crystallinity [71]. Since the grain size decreased with increasing sputtering power, the crystallinity of the films was expected to decrease with increasing sputtering power. To confirm this, the crystallinity of the Ag films was analyzed by XRD.

Figure 3.4 shows the XRD data of Ag films deposited at sputtering powers of 10, 20, 50 100, 200 and 300 W in the 2θ range of $35^\circ - 50^\circ$. The peaks at $2\theta = 38.11^\circ$ and 44.27° indicate the (111) and (200) orientations of Ag, respectively. The crystallinity was examined based on the full width at half maximum (FWHM) intensity of the (111) peak, and using the Scherrer equation:

$$\tau = \frac{K\lambda}{\beta \cos \theta} \quad (3.1)$$

where τ is the mean grain size, K is a dimensionless shape factor, λ is the X-ray wavelength of Cu $K\alpha 1$, β is the FWHM and θ is

the Bragg angle. Equation (3.1) shows that β is inversely proportional to τ . Therefore, the smaller the FWHM, the better the crystallinity [59]. Table 3.4 shows the FWHM values of the Ag films deposited at sputtering powers.

As shown in Figure 3.4 and Table 3.4, the Ag film deposited at the sputtering power of 10 W exhibits the highest (111) peak intensity and smallest FWHM value, of 0.36. Notably, the film deposited at 200 W, rather than the film deposited at 20 W, has the second best crystallinity, with an FWHM value of 0.38, while the film deposited at 300 W has the third best crystallinity with a FWHM value of 0.41. The films deposited at 20, 50 and 100 W have the same FWHM value, of 0.46. However, the (111) peak intensity is highest for the film deposited at 100 W, which has the fourth best crystallinity.

The Ag film deposited at 10 W was predicted to have the highest crystallinity, because it had the largest grain size (see Figure 3.3(a)). This prediction was confirmed, as this film had the lowest FWHM value (see Table 3.4). However, the prediction that the smallest grain sizes identified in the films deposited at 200 and 300 W in Figure 3.3(e) and (f) would correspond to the poorest crystallinities was

not supported; the films deposited at 200 and 300 W had the second and third lowest FWHM values, as shown in Table 3.4. To determine why the grain size results were not in agreement with the FWHM values, the resistivity of the deposited films was measured using a four-point probe.

Figure 3.5 shows the resistivities of the Ag films, which were 4.93 ± 0.11 , 7.61 ± 0.33 , 7.89 ± 0.64 , 6.2 ± 0.24 , 5.83 ± 0.19 and $6.16 \pm 0.19 \mu\Omega \cdot \text{cm}$ for sputtering powers of 10, 20, 50 100, 200 and 300 W, respectively. The bulk resistivity of Ag is $1.59 \mu\Omega \cdot \text{cm}$. As expected from the FWHM value, the Ag films deposited at sputtering powers of 10 and 200 W had the lowest and second lowest resistivities, respectively, (4.93 ± 0.11 and $5.83 \pm 0.19 \mu\Omega \cdot \text{cm}$). Therefore, the FWHM value and resistivity of the film deposited at 200 W were unexpected given the grain size of the film (see Figure 3.4(e)). The increased resistivity of $6.16 \pm 0.19 \mu\Omega \cdot \text{cm}$ for the Ag film at the sputtering power of 300 W was due to the damage caused by the high-energy sputtered flux [72].

One possible explanation for this disagreement is that the grain size presumed from the surface morphology shown in Figure 3.3

might be different from the actual grain size of the film, which should be evaluated by reference to grain boundary observations. To analyze the grain boundaries and film quality, the Ag films deposited at 10, 50 and 200 W were observed by TEM, the samples for which were prepared by FIB.

Figure 3.6 shows low-magnification TEM images of the Ag films deposited at sputtering powers of 10, 50 and 200 W, respectively. Figure 3.6(a) and (c) show the single-crystalline region without grain boundaries, whereas Figure 3.6(b) shows the polycrystalline region with grain boundaries, stacking faults and dislocations.

The characteristics are more clearly visible in the high-resolution TEM and fast Fourier transform (FFT) images shown in Figure 3.7. The (111) lattice and FFT images in Figure 3.7(a) and (c) confirm that the Ag films were single-crystalline and free of defects, with a 3C-Ag face-centered cubic (FCC) structure. Although other areas of the Ag films deposited at 10 and 200 W had some grain boundaries and dislocations, they were very infrequent compared to the Ag film deposited at 50 W.

The (111) lattice and FFT images in Figure 3.7(b) confirm that the Ag film consisted of three grains with different orientations. The lattice image of the square area designated as '1' in Figure 3.7(b) revealed that the lattice was misaligned because of stacking faults, in turn, due to a high number of (111) dislocations. It should be noted that the (200) peaks in the FFT images in Figure 3.7(a) and (c) are shown as points, whereas the (200) and (400) peaks in the FFT images in Figure 3.7(b) are shown as lines, indicating elongation of the (200) and (400) planes caused by multiple stacking faults at various intervals. The lattice and FFT images of the square area designated as '2' in Figure 3.7(b) revealed that the 3C (FCC) and 4H (hexagonal close-packed (HCP)) stackings coexist, with the red triangles and yellow circles in the figure representing the HCP and FCC lattices, indicating the presence of stacking faults [73]. It should be noted that the $(10\bar{1}4)$ peak in the FFT image of Figure 3.7(b) is unique to the HCP structure [74]. Figure 3.8 shows the poly-type structure of Ag. Therefore, grain boundaries, dislocations and stacking faults existed in the Ag film deposited at a sputtering power of 50 W, as shown in Figure 3.7(b).

Figure 3.7 indicates that the density of defects such as grain

boundaries, stacking faults and dislocations in the Ag films increases as the sputtering power increases from 10 to 50 W, and decreases as the sputtering power increases from 50 to 200 W. It is intuitive that the defect density increases as the sputtering power increases from 10 to 50 W, as Ag clusters are expected to be formed during the sputtering process as the sputtering power increases. Ag clusters can be directly sputtered from the target, or formed in the gas phase via collisions among sputtered atoms. However, it is difficult to understand why the defect density decreases as the sputtering power increases from 50 to 200 W, because it is expected that larger Ag clusters are formed in the sputtering process at 200 W compared to 50 W.

One possible explanation is that larger Ag clusters can be more easily charged than smaller Ag clusters, because the ionization potential and electron affinity of large Ag clusters approach the work function of bulk Ag, whereas those of smaller Ag clusters, such as dimers and trimers, approach the ionization potential and electron affinity of a single Ag atom. In other words, the ionization potential and electron affinity of larger Ag clusters would be much smaller and larger, respectively, than those of smaller Ag clusters. As a result,

the probability of positive or negative charging of larger Ag clusters would be much higher than that of smaller Ag clusters. According to the theory of CNPs suggested by Hwang [8], charged clusters less than ~ 2 nm in size tend to be liquid-like because the bond strength is weakened by charge.

From this possibility, the following scenario can be proposed. At a sputtering power of 10 W, the sputtered flux would be relatively small and would mostly consist of single atoms, producing the Ag film with the highest quality, although at an extremely low growth rate. At a sputtering power of 50 W, the sputtered flux would be moderate and there would be some clusters, which would lead to the generation of defects such as grain boundaries, stacking faults and dislocations; the growth rate would be moderate. At a sputtering power of 200 W, the sputtered flux would be relatively large and more clusters would be formed, some of which would be large enough to be charged. These charged clusters would be liquid-like, producing a high-quality film. The growth rate of the film would also be relatively high. Under some conditions, the quality of a thin film deposited at a very high rate may be better than that of a thin film deposited at a low rate [75]. At a sputtering power of 300 W, the sputtered flux would be

large and more clusters would be formed than at the sputtering power of 200 W. However, since the energy of the sputtered flux is high at this sputtering power, the growth rate of the Ag film is reduced and the damage is caused by resputtering, which deteriorates the film quality.

According to this scenario, most of the flux at a plasma power of 10 W would be neutral, whereas some of the flux at a plasma power of 200 W would be electrically charged. An intermediate fraction of the flux would be charged at a plasma power of 50 W. If some flux is charged, the deposition behavior would be affected by the bias applied to the substrate. It is therefore necessary to measure the effect of the charge under a plasma power of 200 W. To investigate the charge effect, thin films were deposited for 20 min while applying biases of +300, 0 and -300 V to the substrate at a plasma power of 200 W, and the same experiment was performed at a plasma power of 10 W for comparison. Since the deposition rate was very slow at the plasma power of 10 W, the film was deposited for 420 min.

Figure 3.9 shows Ag films deposited with substrate biases of -300, 0 and +300 V, respectively, at a sputtering power of 10 W. The

film thicknesses in Figure 3.9 are 64.4 ± 1.1 , 64.4 ± 1.8 and 63.0 ± 2.7 nm, respectively. The thickness of the Ag films was not greatly affected by the substrate bias, indicating that most of the flux is neutral at the sputtering power of 10 W.

At the plasma power of 200 W, however, the thickness of the Ag films was affected by the substrate bias, as shown in Figure 3.10. The Ag films deposited under the substrate biases of -300 , 0 , and $+300$ V had thicknesses of 68.9 ± 2.3 , 77.6 ± 1.4 and 83.5 ± 3.6 nm, respectively. The maximum and minimum film thicknesses were observed at substrate biases of $+300$ and -300 V, respectively. These results indicate that some of the sputtered Ag flux is negatively charged, and the percentage of the Ag sputtered flux that is positively charged is negligibly small.

The film thickness of 68.9 ± 2.3 nm deposited at -300 V is 11.2% less than that of 77.6 ± 1.4 nm deposited at 0 V, indicating that $\sim 11\%$ of the sputtered flux is repelled by the bias of -300 V. The film thickness of 83.5 ± 3.6 nm deposited at $+300$ V is 7.6 % larger than that of 77.6 ± 1.4 nm deposited at 0 V, indicating that $\sim 8\%$ of the sputtered flux is attracted by the bias of $+300$ V. According to these

results, roughly 10% of the flux is negatively charged.

3.4 Conclusion

The growth rate and quality of Ag films were affected by the sputtering power during deposition by DC magnetron sputtering. When the sputtering power is 10 W, most of the flux appears to be in the form of individual atoms, producing the highest quality film but with the lowest growth rate. At a sputtering power of 200 W, a relatively high film quality was obtained at the highest film growth rate. The degradation of film quality with increasing sputtering power is attributed to the generation of neutral clusters during sputtering. The improvement of film quality with a further increase in sputtering power is attributed to the generation of charged clusters during sputtering. The most important finding of this paper is that the charge plays an important role in the deposition of Ag films and that if the fraction of charged clusters is increased, the high quality film can be grown at a high deposition rate.

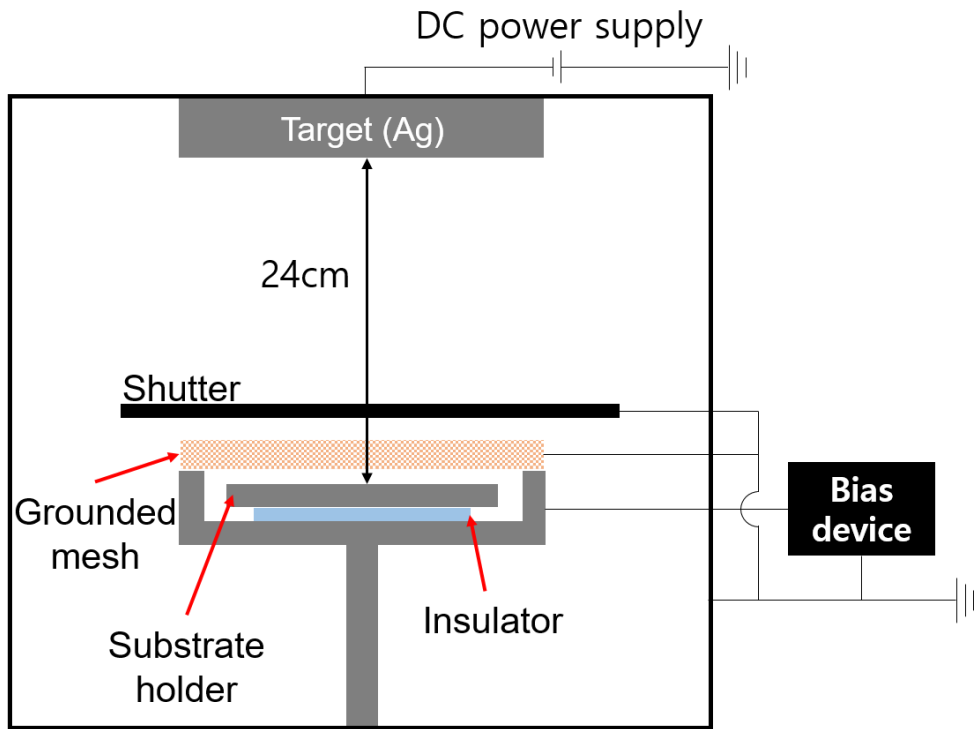


Figure 3.1. Schematic of DC magnetron sputtering chamber.

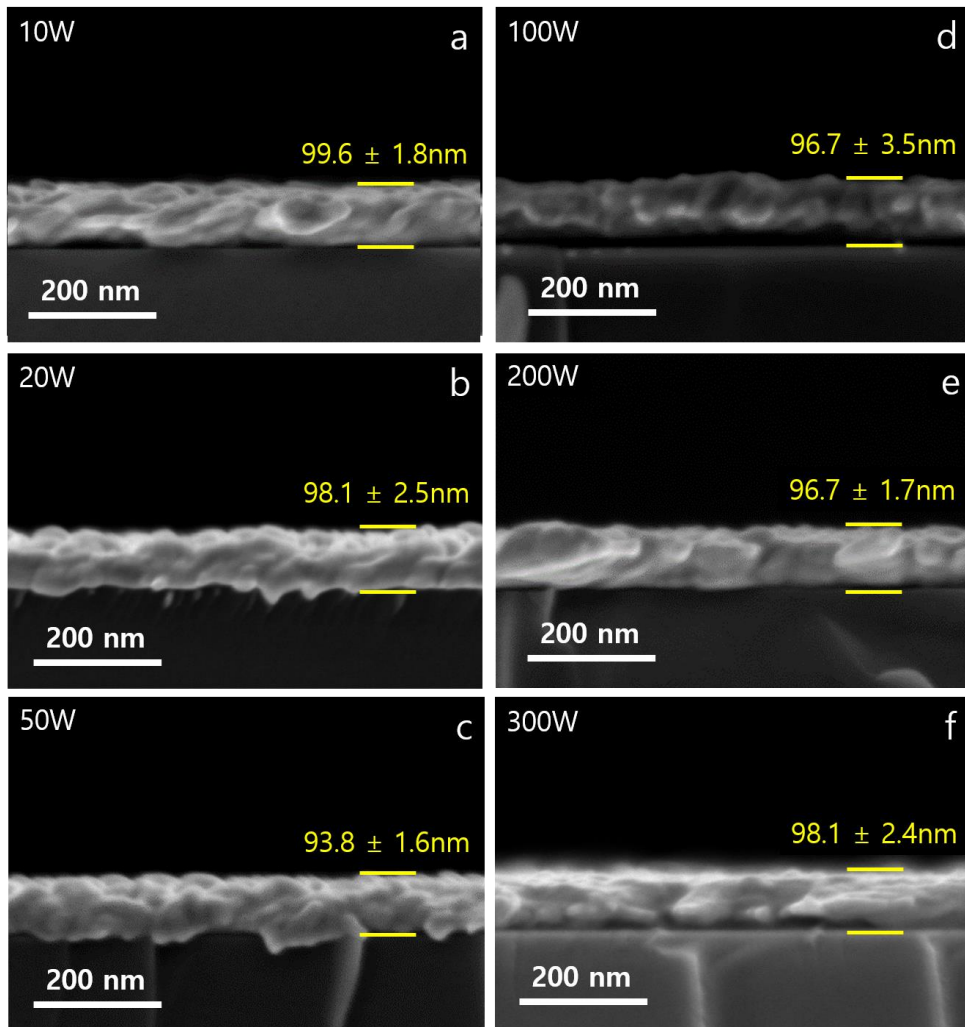


Figure 3.2 Cross-sectional FESEM images of Ag films deposited on Si substrates at sputtering powers of (a) 10 W (b) 20 W (c) 50 W (d) 100 W (e) 200 W and (f) 300 W.

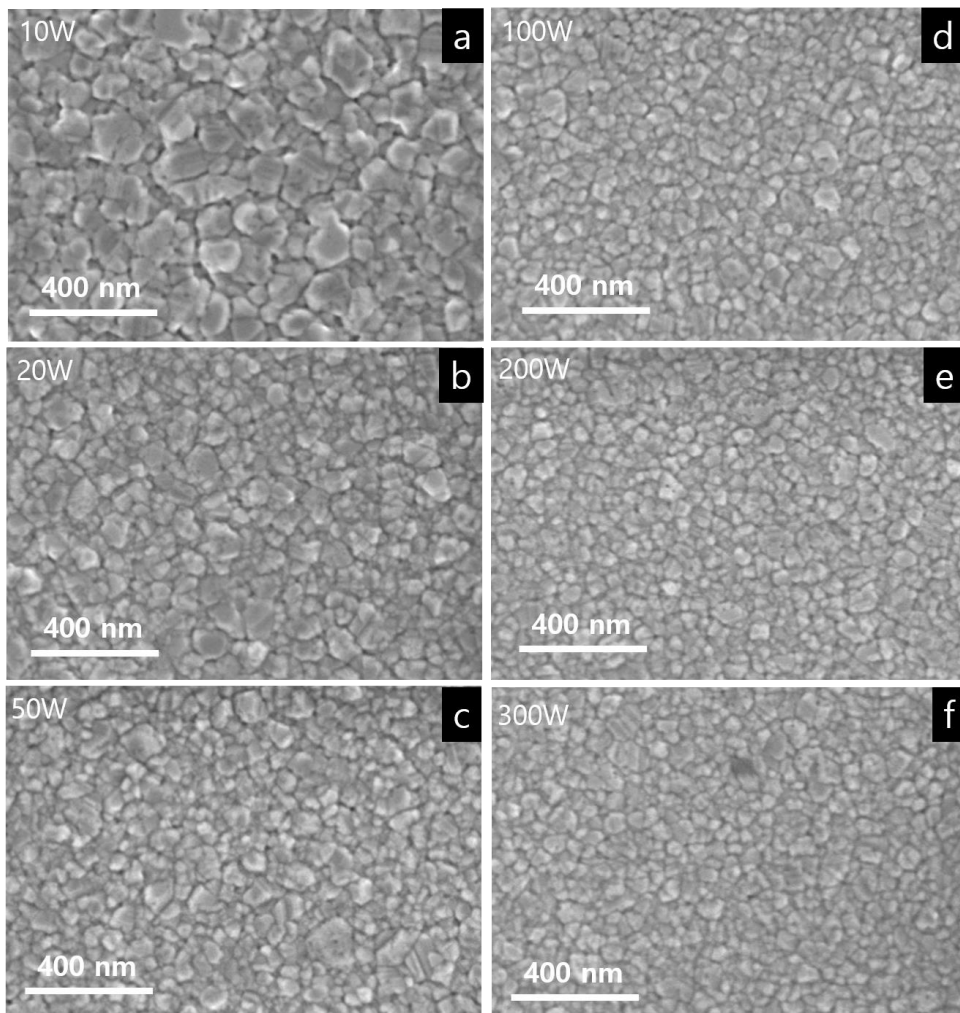


Figure 3.3 Top-view FESEM images of the Ag films deposited on Si substrates at sputtering power of (a) 10 W (b) 20 W (c) 50 W (d) 100 W (e) 200 W and (f) 300 W.

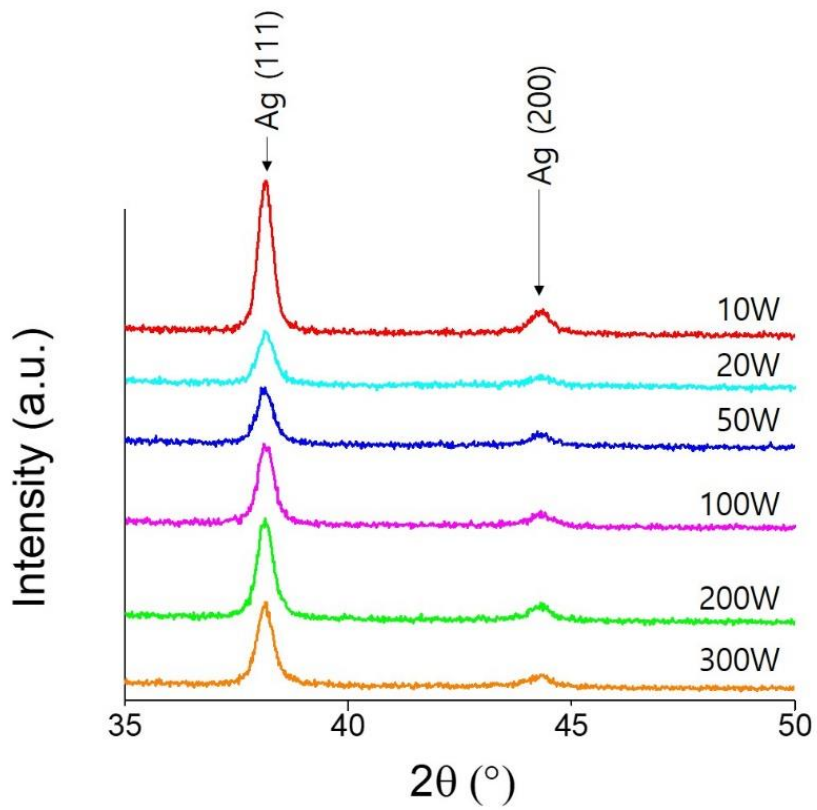


Figure 3.4 XRD data of the Ag films deposited at the sputtering power of 10, 20, 50, 100, 200 and 300 W in the 2θ range of 35° – 50° .

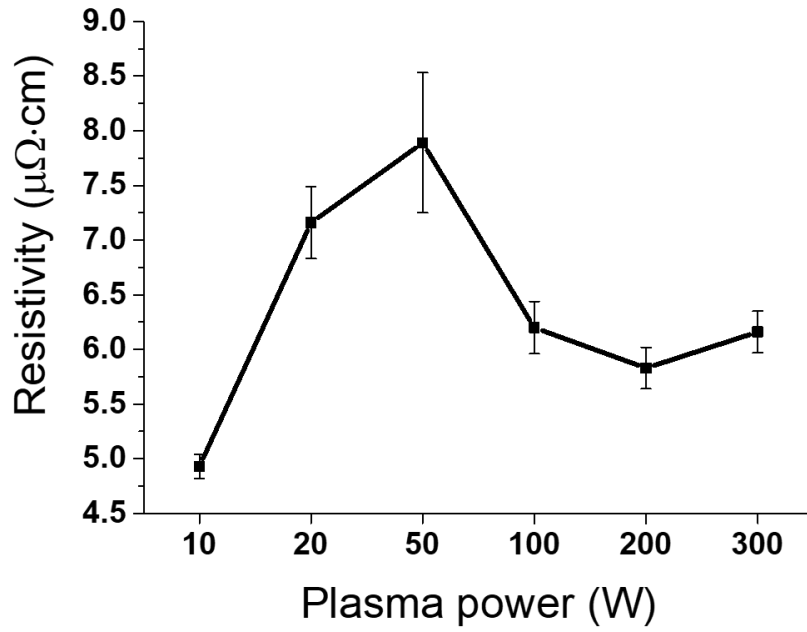


Figure 3.5 Resistivity of the Ag films deposited at the sputtering power of 10, 20, 50, 100, 200 and 300 W.

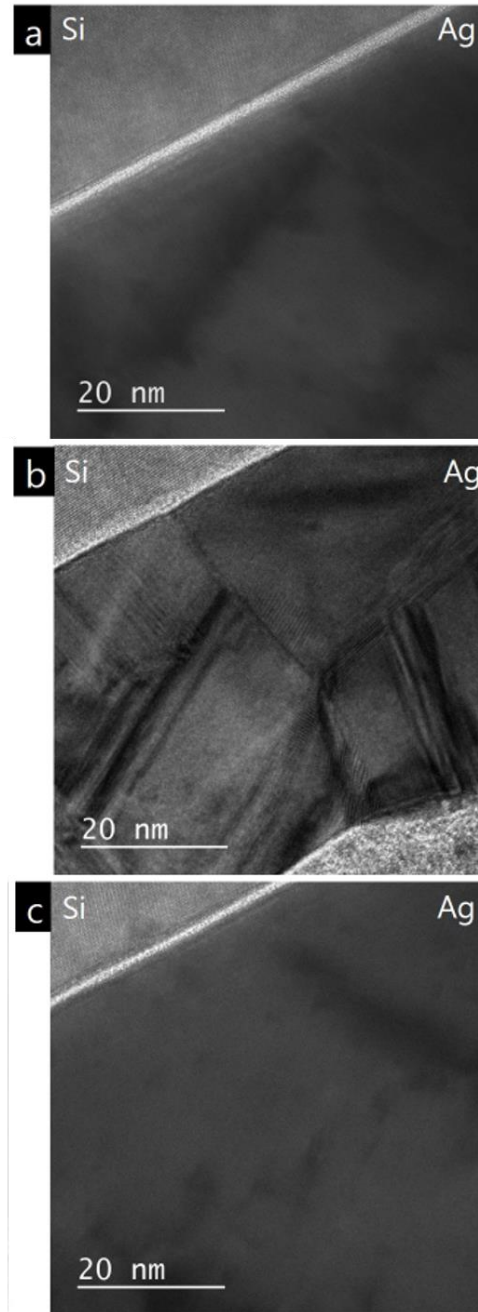


Figure 3.6 Low-magnification TEM images of Ag films deposited on Si substrates at sputtering powers of (a) 10 W (b) 50 W and (c) 200 W.

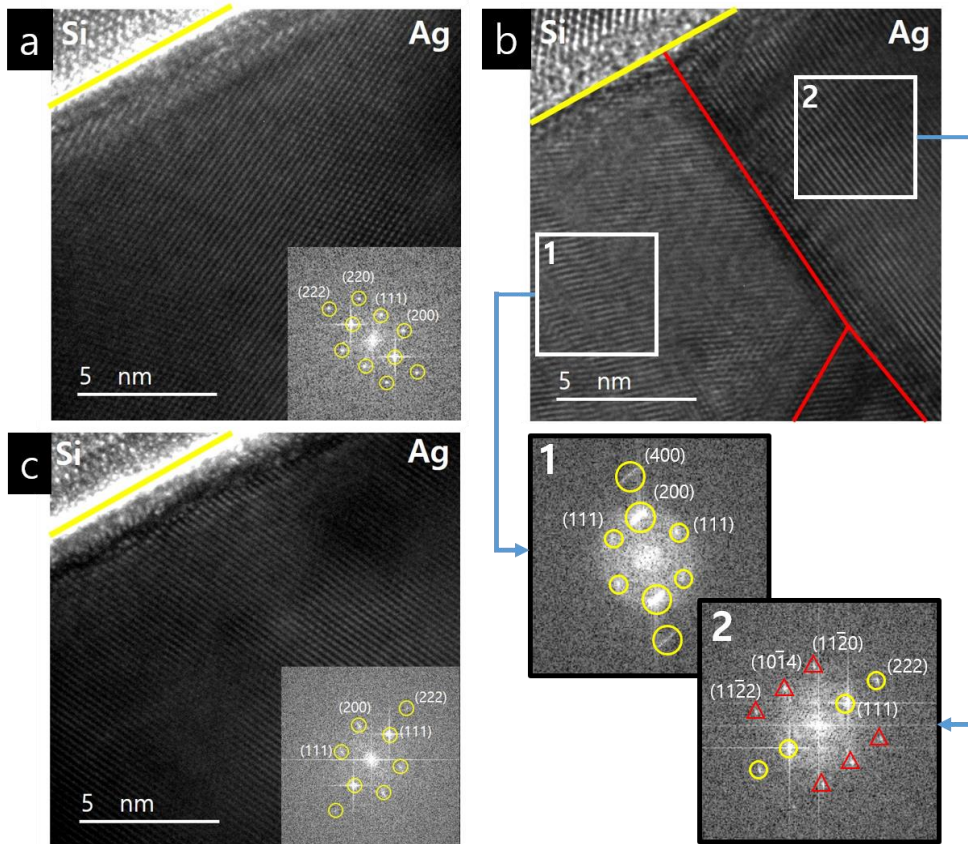


Figure 3.7 HRTEM and FFT images of Ag films deposited on Si substrates at sputtering power of (a) 10 W (b) 50 W and (c) 200 W. The triangle mark is a peak of 4H-Ag HCP and the circle mark is a peak of 3C-Ag FCC in FFT images.

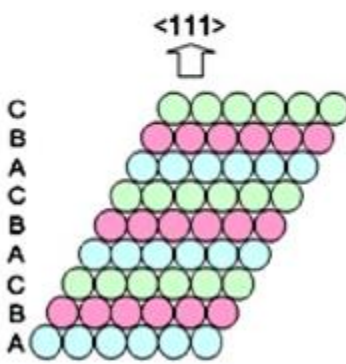
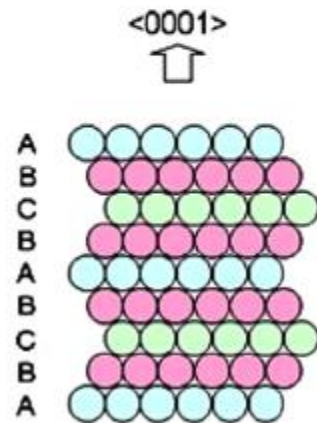
Polytype	3C-silver	4H-silver
Symmetry	Cubic ($Fm\bar{3}m$)	Hexagonal ($P6_3/mmc$)
Lattice parameter (nm)	$a = 0.409$	$a = 0.288, c = 1.000$
Volume/atom (nm^3)	0.017	0.018
Density (g cm^{-3})	10.46	9.97
Interplanar spacing (nm)	0.236	0.250
Stacking sequence of hcp planes	 <p>C B A C B A C B A</p>	 <p>A B C B A B C B A</p>

Figure 3.8 Summary of structural parameters of the 3C and 4H modifications of silver.

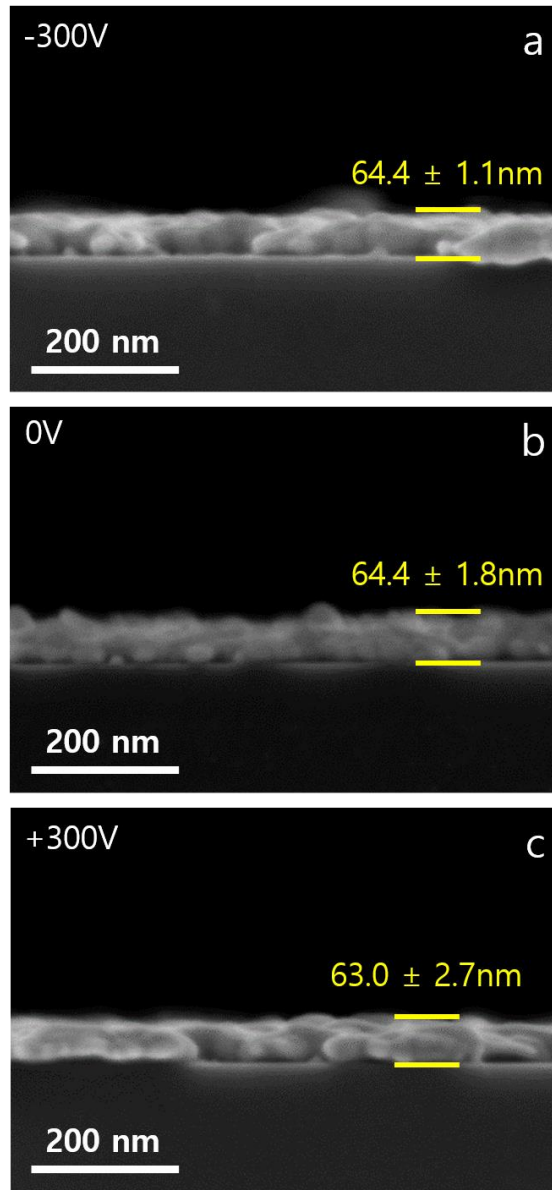


Figure 3.9 Cross-sectional FESEM images of Ag films deposited on Si substrates at the electric biases of (a) -300 V (b) 0 V and (c) +300 V with a sputtering power of 10 W.

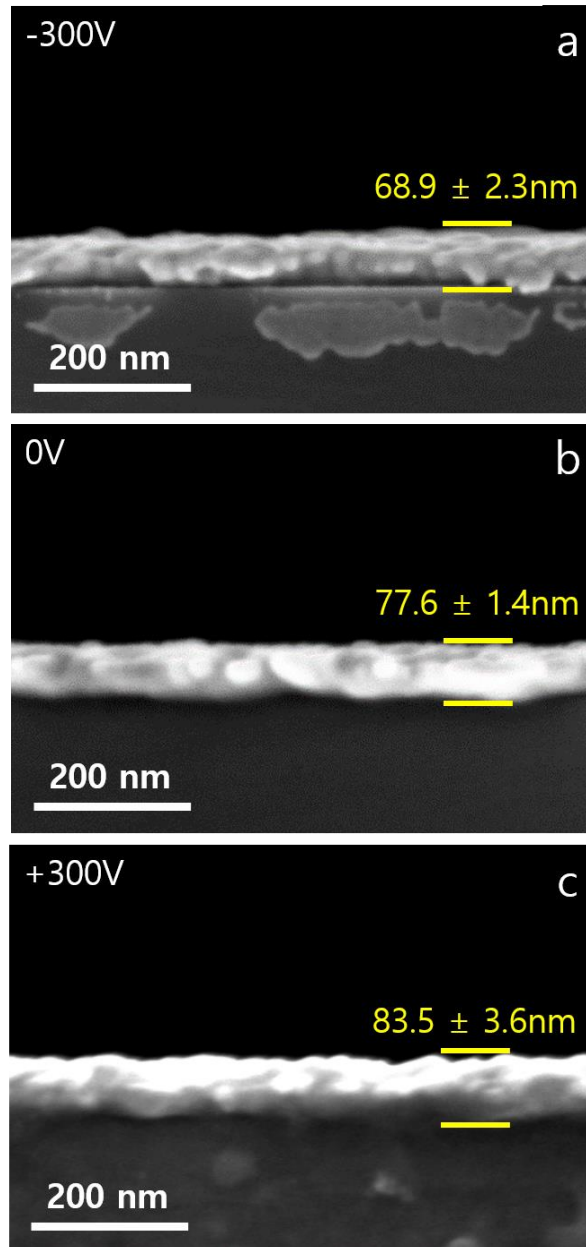


Figure 3.10 Cross-sectional FESEM images of Ag films deposited on Si substrates at the electric biases of (a) -300 V (b) 0 V and (c) +300 V with a sputtering power of 200 W.

	10 W	20 W	50 W	100 W	200 W	300 W
Deposition time (min)	700	210	90	50	25	28

Table 3.1 Deposition time for ~100nm film thickness for each sputtering power.

	10 W	20 W	50 W	100 W	200 W	300 W
Growth rate (nm/min)	0.14 ± 0.002	0.44 ± 0.01	1.04 ± 0.02	1.93 ± 0.07	3.86 ± 0.06	3.50 ± 0.08

Table 3.2 The film growth rate for each sputtering power.

	10 W	20 W	50 W	100 W	200 W	300 W
Grain size (nm)	134 ± 27	87 ± 13	67 ± 8	51 ± 6	47 ± 6	50 ± 4

Table 3.3 Grain size of Ag films deposited on Si substrates for each sputtering power.

	10 W	20 W	50 W	100 W	200 W	300 W
FWHM (°)	0.36	0.46	0.46	0.46	0.38	0.41

Table 3.4 The FWHMs of (111) peaks for each sputtering power.

Chapter 4.

Effect of working pressure on the deposition behavior of Ag films during DC magnetron sputtering considering the generation of charged clusters

4.1. Introduction

The mechanism of crystal growth can be explained as a terrace–ledge–kink (TLK) model [1] that is deposited on the atom, ion or molecular basis. This growth mechanism is called classical crystallization. However, the growth behavior that is difficult to explain with the existing TLK model has been reported. Research to solve these phenomena is ongoing, and many researchers call it a non–classical crystallization and interpret the building blocks of crystal growth as nanoparticles [7, 9, 11, 12, 14, 50, 51, 60–63, 76,

77].

Further here, Hwang et al. [8] has done a lot of research on non-classical crystallization. In particular, they have studied extensively the thin film growth in the chemical vapor deposition (CVD) process. They suggest 'the theory of charged nanoparticles (TCN)' new crystal growth mechanism. The TCN explains that electrically charged nanoparticles are first generated in the gas phase, and these charged nanoparticles are deposited to form a thin film during the CVD process. In this case, the crystal growth unit is nanoparticles, not atoms or molecules, where charge plays a very important role. According to the TCN, if the nanoparticles are neutral, a thin film tends to become porous by random Brownian coagulation, but if they are charged, a thin film tends to become dense by the highly orderly manner of deposition by self-assembly. For example, Park et al. [52] deposited a fully epitaxial silicon film on a silicon wafer at 550 ° C under the substrate bias of -1000 V during radio frequency plasma-enhanced chemical vapor deposition (RF-PECVD). it is due to the liquid-like nature of charged nanoparticles. When the particles are charged, the binding energy between atoms is weakened, so the nanoparticles have high atomic mobility. Clare et al. [30] reported

that the bond strength of Si–H and Si–Si is weakened by the presence of charge in silane (SiH₄) and disilane (Si₂H₆) molecules by the ab initio calculation.

Many studies have been conducted on charged nanoparticles in CVD [8, 64, 78–82]. Reiprich et al. [79] performed localized and programmable CVD using an Electrically Charged and Guided Molecular Flux with charged nanoparticles. Wu et al. [80] studied the gas nucleation process of anatase TiO₂ in atmospheric non-thermal Plasma Enhanced CVD from the perspective of the TCN. Also, Kim et al. [64] confirmed the generation of Charged SiC Nanoparticles During the HWCVD Process.

Recently, research on charged nanoparticles in PVD is actively underway. Jeon et al. [41] confirmed the presence of charged Ag nanoparticles through a bias experiment in the evaporator. Jang et al. [69] studied the existence of charged Ag nanoparticles in DC magnetron sputter and their contribution to Ag film deposition behavior. Also, Kwon et al. [53] studied the existence of charged Ti nanoparticles in RF magnetron sputter and their effect on Ti film deposition behavior. However, a lot of research is still needed in PVD.

In this study, it is to investigate the effect of process parameters on the Ag film growth in DC magnetron sputtering. The Ag films were deposited while varying the process pressure, sputtering power, and bias applied to the substrate. At this time, we intend to understand the growth behavior of the Ag films with the theory of charged nanoparticles. It will confirm the possibility that the charge can act as a new process parameter in the DC magnetron sputtering.

4.2. Experimental methods

Figure 4.1(a) shows a schematic of the DC magnetron sputter. The Ag target of 99.999% purity and 7.62 cm diameter was used. The plasma was generated by a DC power supply (psplasma, Inc., SDC1022A, Hwaseong, South Korea) connected to the Ag target. The distance between the substrate holder and the Ag Target was fixed at 12 cm. The substrate holder, which is electrically floated from the grounded chamber in order to apply the electric bias, was placed on the glass. To minimize the effect of the substrate holder bias on the plasma, the Cu grounded mesh is set up above the substrate holder. The hole size of the grounded Cu mesh was

selected to $150 \mu\text{m}$, which does not exceed the Debye length of the plasma. The shutter was installed above the grounded Cu mesh to control the film deposition time by opening or closing.

To confirm whether any of the sputtered flux is charged, the current of the substrate holder was measured during the DC magnetron sputtering process. The current is measured by a pico-ammeter (KEITHLEY 6487, Tektronix, Cleveland, OH, USA). Figure 4.1 (b) shows the current measured in the substrate holder while the plasma was turned on during the sputtering process. As soon as the plasma was turned on, a negative current was measured, which was approximately $-500 \mu\text{A}$. It means that the negatively charged flux is reaching the substrate. Most will be electrons, but the negatively charged sputtered flux should also be considered. It can be distinguished through an experiment in which a bias is applied to the substrate.

The DC plasma power was varied as 20, 50, 100 and 200 W. The Ag films were deposited while changing the working pressure of 2.5, 5, 10, and 20 mTorr under each plasma power, respectively, at room temperature. To investigate the effect of charged particles on the film

growth, Ag films were deposited while applying the bias of $-300, 0$ and $+300$ V to the substrate holder. The Ag films were deposited for the same time, 30 min. A p-type Si (100) was used for film deposition as a substrate.

To check the size of Ag sputtered particles, a capture experiment was conducted by sputtering for 3 seconds, which is a very short time, on an amorphous carbon transmission electron microscopy (TEM) membrane. The captured Ag particles were observed by TEM (FEI, Tecnai F20, Hillsboro, OR, USA). TEM was operated at an accelerating voltage of 200 kV. TEM images were analyzed using The open source software ImageJ (1.51k, National Institutes of Health, Bethesda, MD, USA).

The microstructure of the Ag films was investigated by field-emission scanning electron microscopy (FESEM) (Carl Zeiss, SUPRA, Oberkochen, Germany) operated at accelerating voltages of 2 kV. The crystallinity of the Ag films is analyzed by X-ray diffraction (XRD) (PANalytical, X'pert-Pro, Almelo, The Netherlands) at a 2θ scanning range of $30\sim 80^\circ$ with the Cu $K\alpha$ ($\lambda=1.5418$ Å) source. The resistivity of Ag films is measured using

a four-point probe (CMT-SR2000N, Materials Development Corporation).

4.3. Results and discussion

Figure 4.2 shows cross-section FESEM images of the Ag films deposited on a Si substrate while changing the working pressure at the sputtering power of 100 W. Thicknesses of the Ag films, determined by the cross-section FESEM images, were 377.9, 281.3, 252 and 190.4 nm, respectively, for the working pressure of 2.5, 5, 10 and 20 mTorr. It was confirmed that the thickness of the Ag films increased as the working pressure decreased. It means that when the working pressure in the chamber is lowered, the mean free path becomes longer. At that time, the number of collisions of argon ions accelerated toward the target decreases. As a result, the loss of the kinetic energy of argon ions is reduced. Therefore, it is possible to sputter the target with strong energy. Since the target is sputtered with strong energy, the sputtering efficiency is increased. As a result, as the working pressure decreases at constant sputtering power, the growth rate of the film increases [83].

To investigate the charge effect during the sputtering, the Ag films were deposited for 30 min while applying biases of +300, 0 and -300 V to the substrate at a sputtering power of 100 W and a working pressure of 2.5 mTorr. As shown in Figure 4.3, the thicknesses of the Ag films were 345.7, 377.9 and 416.0 nm for the biases of -300, 0 and +300 V, respectively. When a positive bias was applied to the substrate, the thickness increased by 10%. And when a negative bias was applied to the substrate, the thickness of the thin film decreased by 8.5%. It is evidence that most of the sputtered Ag flux is negatively charged, and the amount is around 10%.

Figure 4.2 and Figure 4.3 are representative images of the experimental results. The thickness, FWHM and resistivity of 45 Ag films conducted under all experimental conditions were measured. It was summarized as a graph to see the effect of the substrate bias and the working pressure. The deposition behavior of Ag films according to sputtering power is described in detail in Chapter 3.

Figure 4.4 shows the thickness of the Ag films according to the working pressure change while applying a bias to the substrate at each sputtering power. It was confirmed that the thickness of the Ag

films increased as the working pressure decreased under all sputtering power conditions. It can be explained for the same reason as in Figure 4.2.

To confirm the effect of charge, the thickness of the film according to the bias change was summarized in Figure 4.5. In all plasma power conditions, it was confirmed that the thickness of the Ag films increased when the bias applied to the substrate was positive, and the thickness of the Ag films decreased when the bias applied to the substrate was negative. It can also be explained as the reason in Figure 4.3. It should be noted that the ratio of the thickness of the Ag films, which is changed by the substrate bias, varies depending on the process pressure. In Figure 4.5, it can be confirmed by the slope of the graph, but it is summarized in Table 1 to confirm the correct ratio.

Table 4.1 shows the ratio of the thickness change of Ag films when a bias is applied to the substrate. It was confirmed that the rate of thickness change increased as the working pressure decreased under all plasma power conditions. It means that as the working pressure decreases, the amount of sputtered Ag flux affected by the

bias applied to the substrate increases. Therefore, as the working pressure decreases, the amount of negatively charged nanoparticles increases. And it is confirmed that the amount converged to around 10%. Here, the thickness of the Ag film of 20 mTorr at a sputtering power of 20 W and the Ag film of 20 mTorr at a sputtering power of 50 W did not change according to the substrate bias change. This is discussed in detail later.

XRD analysis was performed to confirm the crystallinity of the Ag films. Figure 4.6 shows the FWHM on the (111) plane, which is the main pick of the Ag films according to the working pressure change while applying a bias to the substrate at each sputtering power. The FWHM tends to be different from the thickness. In all plasma power conditions, when the bias applied to the substrate was -300 V, it was confirmed that the FWHM increased as the working pressure decreased, and when the bias applied to the substrate was 0 V and $+300$ V, the FWHM decreased as the working pressure decreased. According to the Scherrer equation, the FWHM is inversely proportional to the crystallinity [59].

$$\tau = \frac{K\lambda}{\beta \cos \theta} \quad (4.1)$$

In Equation 4.1, τ is the mean grain size, K is a dimensionless shape factor, λ is the X-ray wavelength of Cu K α_1 , β is the FWHM and θ is the Bragg angle. Therefore, when the bias applied to the substrate is -300 V, it has poor crystallinity, and when the bias applied to the substrate is 0 V and $+300$ V, it has good crystallinity.

It can be explained by the influence of charged nanoparticles. Considering the charge ratio of the nanoparticles according to the working pressure described above, as the working pressure decreases, the ratio of the charged nanoparticles increases. Therefore, when a positive bias is applied to the substrate, a larger amount of charged nanoparticles will be attracted and the crystallinity of the Ag film will be improved due to the liquid-like property of the charged nanoparticles. On the contrary, when a negative bias is applied to the substrate, a larger amount of charged nanoparticles will be repelled, so the crystallinity of the Ag film will be deteriorated by neutral nanoparticles. There is a different trend at a working pressure of 2.5 mTorr. It is thought to damage the Ag film because

the sputtered nanoparticles reach the substrate with high energy without collision due to a very long mean free path with low working pressure.

Figure 4.7 shows the FWHM organized according to the substrate bias. In all plasma power conditions, when a positive bias was applied to the substrate, the FWHM tended to decrease, and when a negative bias was applied to the substrate, the FWHM tended to increase. It can also be interpreted that the presence or absence of charged nanoparticles with liquid-like properties affects the crystallinity of the Ag film. Therefore, when the working pressure decreases, if the positive bias is applied to the substrate, the FWHM is lowered, resulting in good crystalline film quality. If the negative is applied to the substrate, the FWHM increases, resulting in a poorly crystalline thin film.

The resistivity was measured to confirm the electrical properties of the Ag films. Figure 4.8 shows the resistivity of the Ag films according to the working pressure change while applying a bias to the substrate at each sputtering power. The resistivity shows the same change pattern as the FWHM. In all sputtering power conditions,

when a bias of -300V was applied to the substrate, it was confirmed that the resistivity increased as the working pressure decreased. Also, when biases of 0V and $+300\text{V}$ were applied to the substrate, it was confirmed that the lower the working pressure, the lower the resistivity. This result means that the resistivity is proportional to the crystallinity.

the resistivity of the Ag films according to the bias change was summarized in Figure 4.9. In all sputtering power conditions, when a positive bias was applied to the substrate, the resistivity tended to decrease, whereas when a negative bias was applied to the substrate, the resistivity tended to increase. This result can be explained by the influence of charged nanoparticles, similar to the FWHM described above.

Summarizing the above analysis results, such as thickness, FWHM and resistivity, the quality of the deposited film was improved under conditions in which a lot of charged Ag particles were present. Then, if the above results were produced by the influence of charged nanoparticles, you would be curious about the correlation between the working pressure and charged nanoparticles. In chapter 3, it

suggested the possibility that sputtering power affects the sputtered particle size, and this size change affects the possibility of charging. Accordingly, it can be considered that the working pressure also affected the size change of the sputtered particles.

As the working pressure increases, the mean free path in the chamber is shortened. Collisions between particles increase due to the shorter mean free path. The number of collisions of argon ions accelerated to the target for sputtering increases, resulting in a large loss of kinetic energy. Argon, which has lost a lot of energy, hits the target with little force. Therefore, it is thought that small-sized particles will be sputtered. As the process pressure gradually decreases, the mean free path in the chamber increases and argon accelerated to the target also sputters with large energy with little energy loss. As a result, large sputtered particles are created.

The difference in the size of nanoparticles makes the possibility of being charged differently. The small sputtered Ag particles, such as dimers and trimers, are difficult to be charged because of the electron affinity and ionization of those approaches to a single Ag atom. Whereas, the large sputtered Ag particles are easy to be

charged because of the electron affinity and ionization of those approaches to the work function of bulk Ag. Eventually, the charged large sputtered Ag particles form a high-quality Ag film due to their liquid-like properties. And neutral small sputtered Ag particles form low quality Ag films by random Brownian coagulation.

Through the capture experiment, the size of the sputtered nanoparticles was confirmed according to the working pressure change. Figure 4.10 shows TEM images of the sputtered Ag particles according to the working pressure changes at the sputtering power of 100 W and the substrate bias of 0 V. Sputtered Ag particles captured for 2.5, 5, 10 and 20 mTorr had the average sizes of 17.9 ± 0.0 , 17.2 ± 0.0 , 15.1 ± 0.0 and 11.3 ± 0.0 nm, respectively. It was confirmed that the size of the nanoparticles increased as the working pressure decreased.

For this reason, as shown in Table 4.1, it can be explained that the proportion of charged Ag particles increases as the working pressure decreases. And the thickness variation of the Ag film was little by the bias of the substrate at a sputtering power 20W and 50W, the working pressure 20mTorr condition in Table 4.1. Because the

sputtered nanoparticles are very small when the working pressure is high, it is difficult to be charged. Therefore, since it exists as a neutral particle, it is not affected by the substrate bias.

4.4. Conclusion

The deposition behavior of Ag film was confirmed while changing the process parameters such as working pressure, substrate bias and sputtering power during DC magnetron sputtering. As the working pressure decreased, the growth rate of the Ag films increased, and the size of the sputtered Ag particles was large. On the other hand, as the working pressure increased, the growth rate of the thin film was slow, and the size of sputtered Ag particles was small. The difference in the size of the Ag particles according to the working pressure changed the possibility of the particles being charged. The proportion of charged particles was confirmed by the bias applied to the substrate. The high quality Ag films were made when lots of charged particles existed. Therefore, the charge plays an important role in the film deposition behavior, and the possibility of a new process parameter in DC magnetron sputter was confirmed.

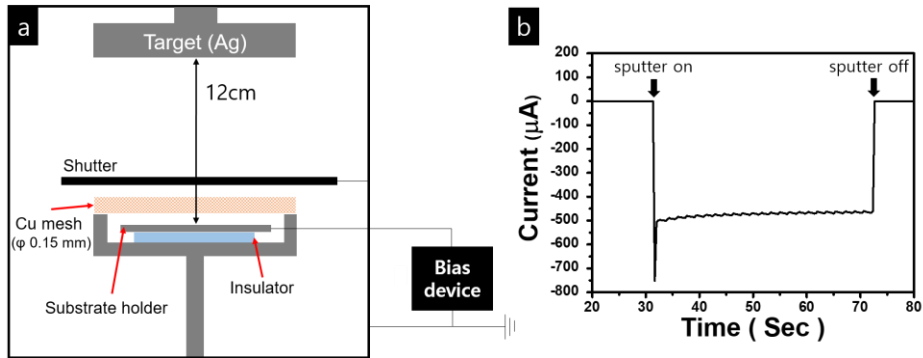


Figure 4.1. (a) Schematic of the DC magnetron sputtering chamber and (b) the current measured on the substrate holder at the plasma power of 100 W.

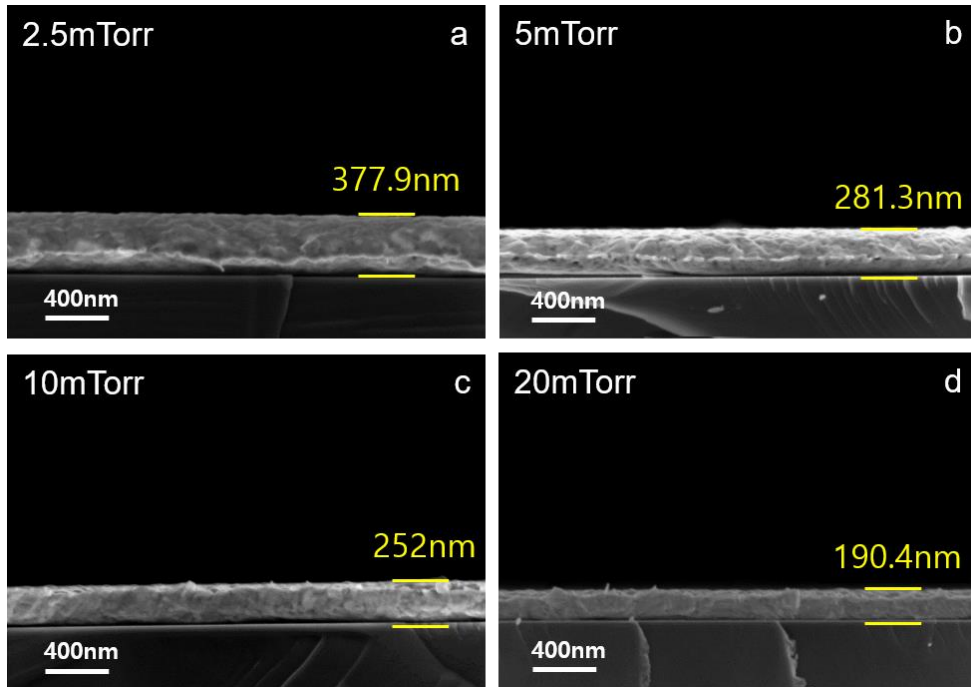


Figure 4.2. Cross-section FESEM images of the Ag films deposited on Si substrates at the working pressure of (a) 2.5 mTorr; (b) 5 mTorr; (c) 10 mTorr; and (d) 20 mTorr at the sputtering power of 100 W.

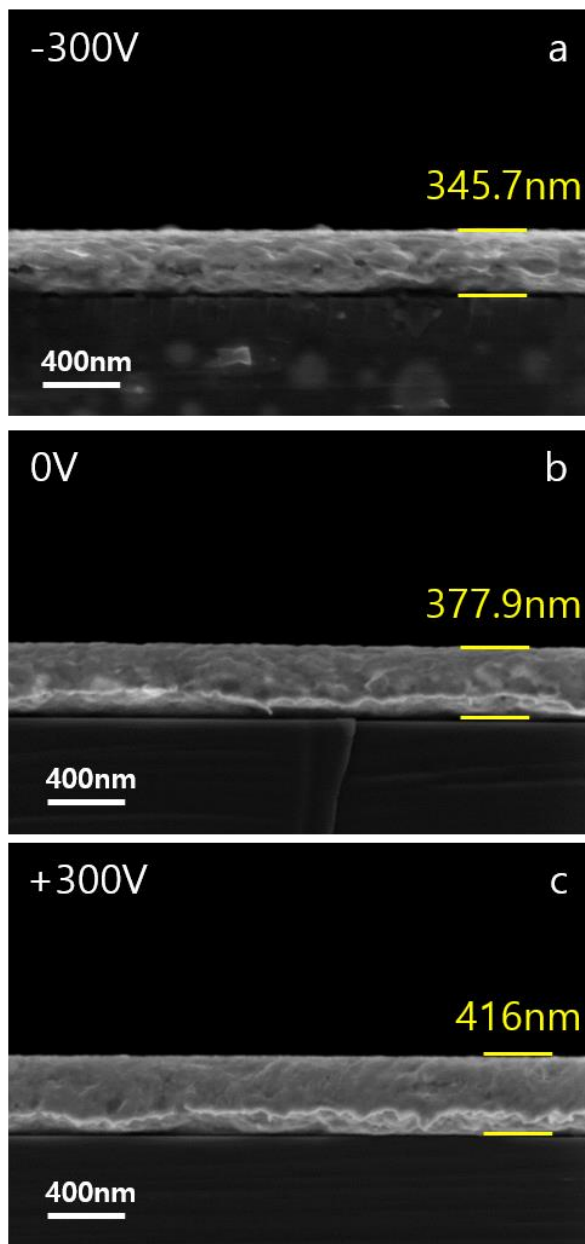


Figure 4.3. Cross-section FESEM images of the Ag films deposited on Si substrates at the electric biases of (a) -300 V; (b) 0 V; and (c) $+300$ V at the working pressure of 2.5 mTorr and the sputtering power of 100 W.

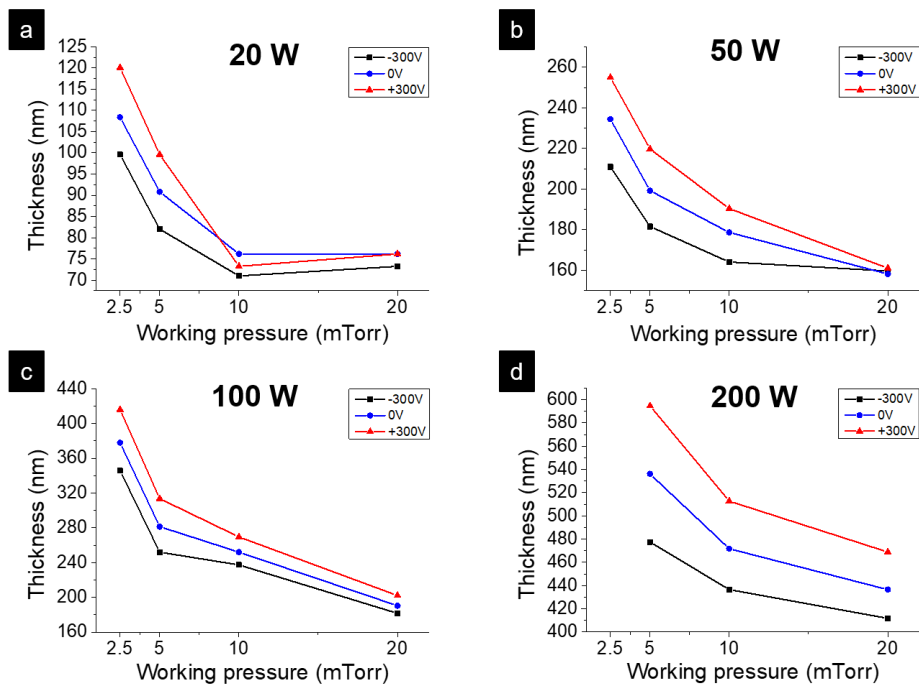


Figure 4.4. Plots of the thickness of Ag films according to the working pressure change while applying a bias to the substrate at sputtering power of (a) 20 W; (b) 50 W; (c) 100 W; and (d) 200 W.

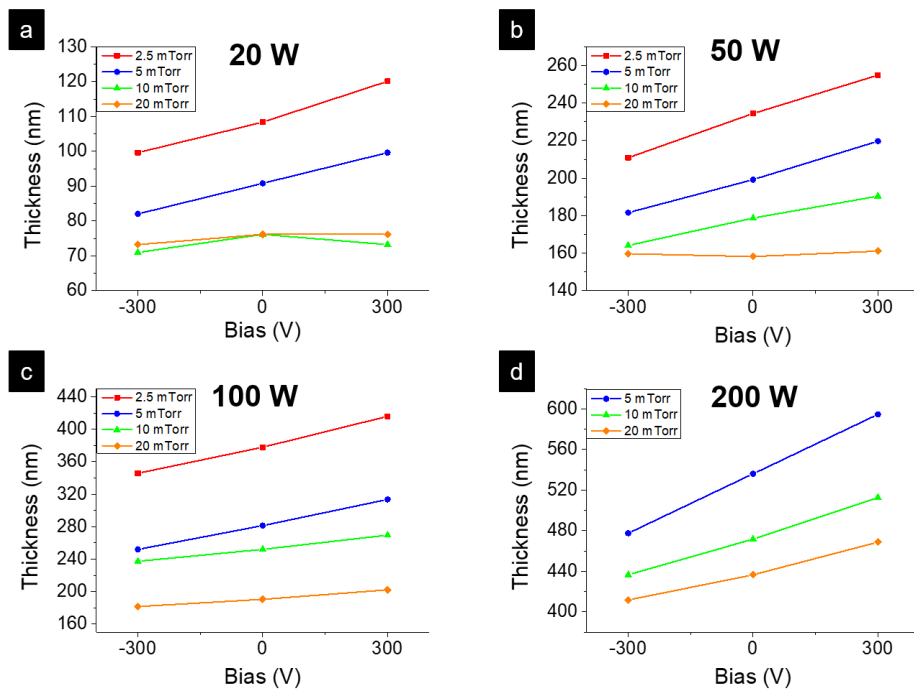


Figure 4.5. Plots of the thickness of Ag films according to the substrate bias change while changing the working pressure at the sputtering power of (a) 20 W; (b) 50 W; (c) 100 W; and (d) 200 W.

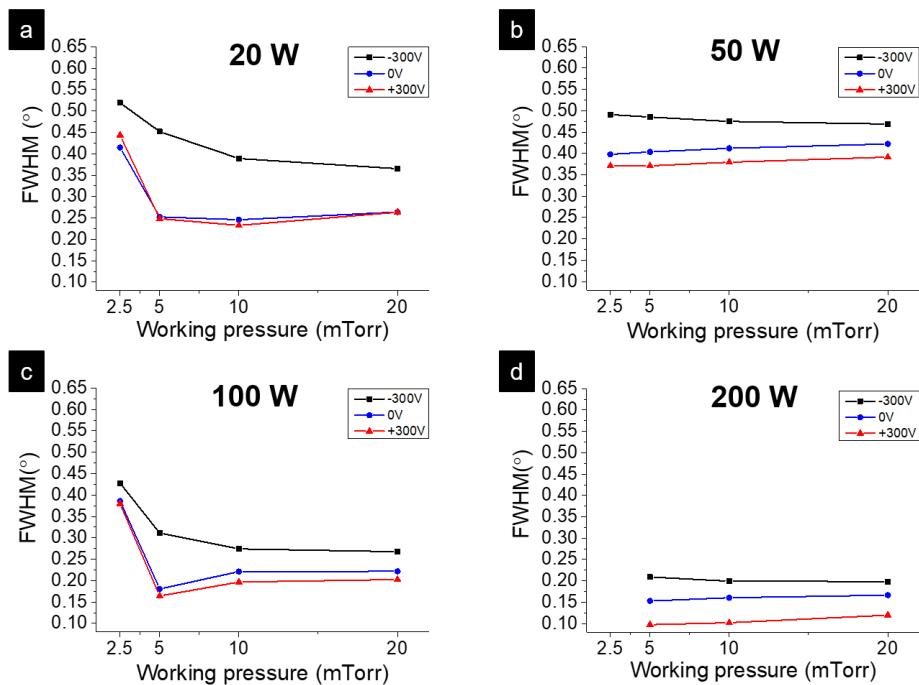


Figure 4.6. Plots of the FWHM of Ag films of (111) peak according to the working pressure change while applying a bias to the substrate at sputtering power of (a) 20 W; (b) 50 W; (c) 100 W; and (d) 200 W.

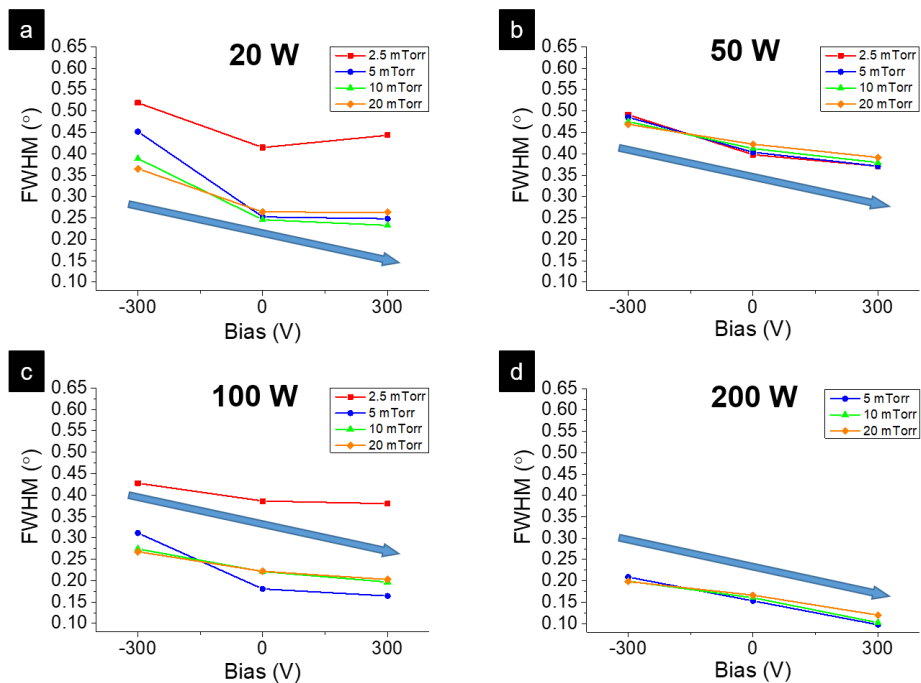


Figure 4.7. Plots of the FWHM of Ag films of (111) peaks according to the substrate bias change while changing the working pressure at the sputtering power of (a) 20 W; (b) 50 W; (c) 100 W; and (d) 200 W.

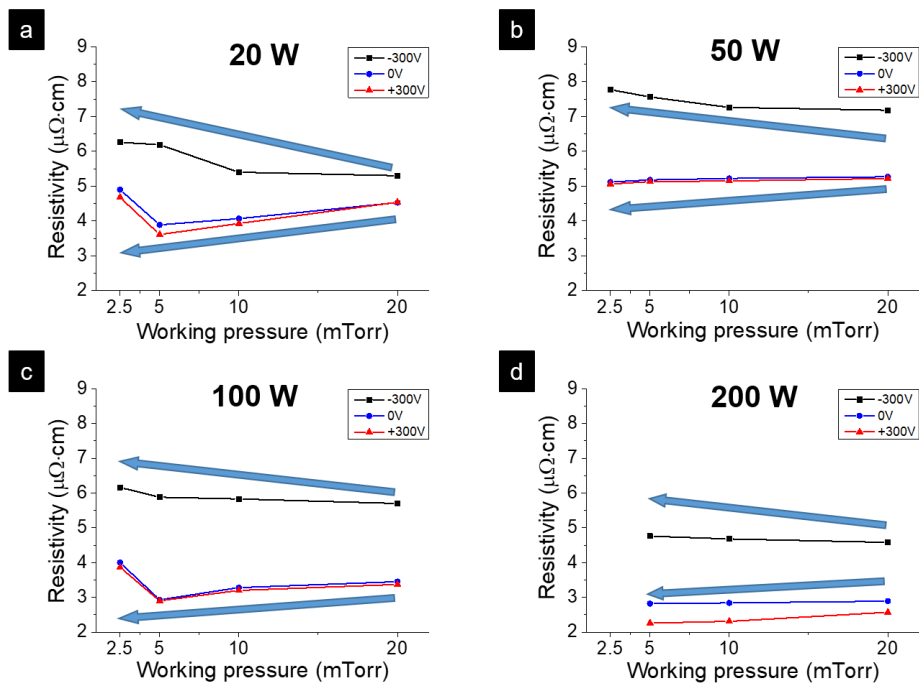


Figure 4.8. Plots of the resistivity of Ag films according to the working pressure change while applying a bias to the substrate at sputtering power of (a) 20 W; (b) 50 W; (c) 100 W; and (d) 200 W.

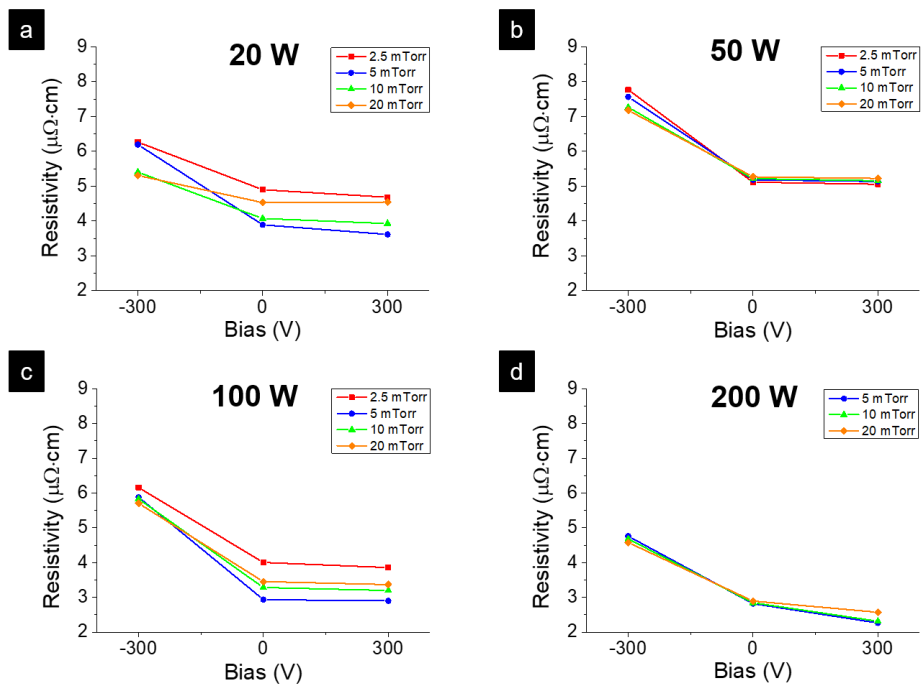


Figure 4.9. Plots of the resistivity of Ag films according to the substrate bias change while changing the working pressure at the sputtering power of (a) 20 W; (b) 50 W; (c) 100 W; and (d) 200 W.

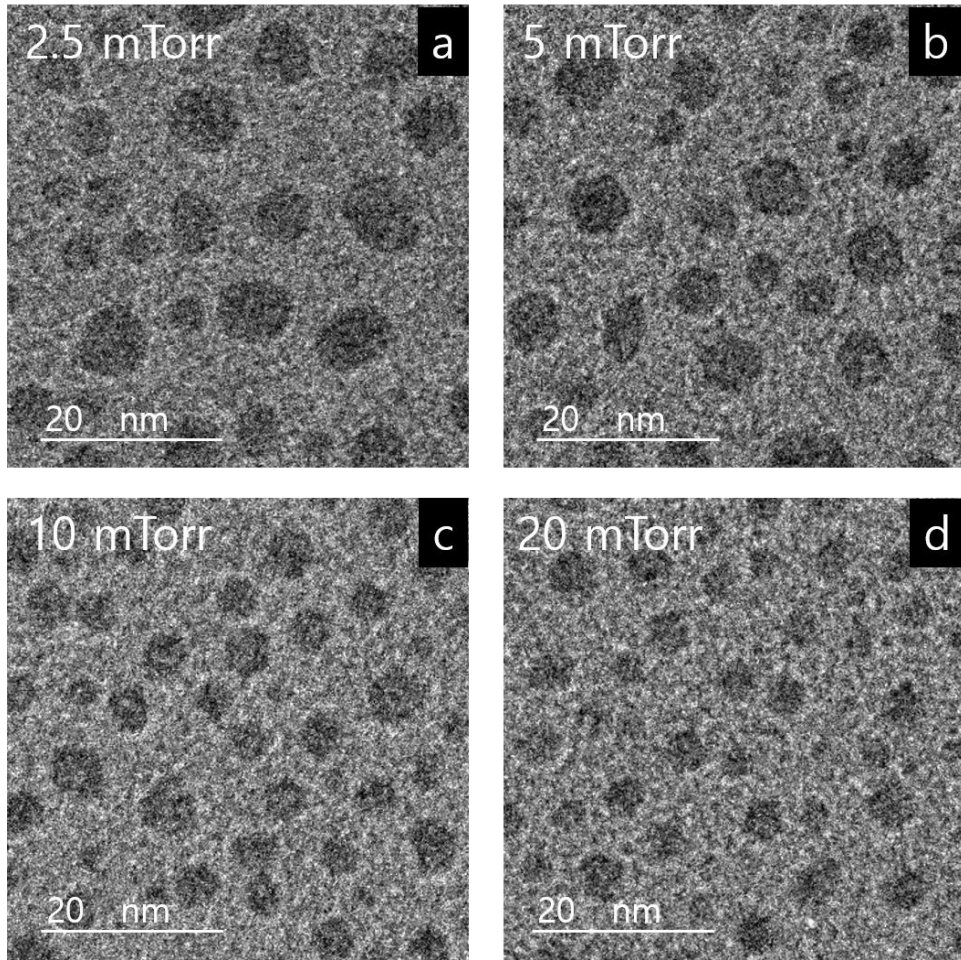


Figure 4.10. TEM images of Ag particles captured on an amorphous carbon membrane at the working pressure of (a) 2.5 mTorr; (b) 5 mTorr; (c) 10 mTorr; and (d) 20 mTorr at the sputtering power of 100 W and the substrate bias of 0 V.

20 W	-300 V	0 V	+300 V
2.5 mTorr	-8.1	-	+10.7
5 mTorr	-9.6	-	+9.6
10 mTorr	-6.8	-	-3.8
20 mTorr	-3.4	-	0

(a)

50 W	-300 V	0 V	+300 V
2.5 mTorr	-10.0	-	+8.7
5 mTorr	-8.8	-	+10.2
10 mTorr	-8.1	-	+6.5
20 mTorr	0.9	-	+1.8

(b)

100 W	-300 V	0 V	+300 V
2.5 mTorr	-8.5	-	+10.0
5 mTorr	-10.4	-	+11.44
10 mTorr	-5.8	-	+6.9
20 mTorr	-4.6	-	+6.1

(c)

200 W	-300 V	0 V	+300 V
2.5 mTorr	-	-	-
5 mTorr	-10.9	-	+10.9
10 mTorr	-7.4	-	+8.6
20 mTorr	-5.6	-	+7.3

(d)

Table 4.1. The ratio of the thickness change of Ag films when a bias is applied to the substrate at sputtering power of (a) 20 W; (b) 50 W; (c) 100 W; and (d) 200 W.

Reference

- [1] I.V. Markov, *Crystal Growth for Beginners*, World Scientific, 2003.
- [2] A.A. Howling, L. Sansonnens, J.L. Dorier, C. Hollenstein, Negative hydrogenated silicon ion clusters as particle precursors in RF silane plasma deposition experiments, *Journal of Physics D: Applied Physics*, 26 (1993) 1003–1006.
- [3] S. Vepřek, O. Ambacher, W. Rieger, K. Schopper, M.G.J. Vepřek–Heijman, Clusters in A Silane Glow Discharge: Mechanism of Their Formation and How to Avoid Them, *MRS Proceedings*, 297 (1993) 13.
- [4] A. Garscadden, B.N. Ganguly, P.D. Haaland, J. Williams, Overview of growth and behaviour of clusters and particles in plasmas, *Plasma Sources Science and Technology*, 3 (1994) 239–245.
- [5] E. Stoffels, W.W. Stoffels, G.M.W. Kroesen, F.J. de Hoog, Dust formation and charging in an Ar/SiH₄ radio-frequency discharge, *Journal of Vacuum Science & Technology A*, 14 (1996) 556–561.
- [6] F.F. Amos, L. Dai, R. Kumar, S.R. Khan, L.B. Gower, Mechanism of formation of concentrically laminated spherules: implication to Randall’ s plaque and stone formation, *Urological Research*, 37 (2009) 11–17.
- [7] X. Feng, R. Gao, R. Wang, G. Zhang, Non–classical crystal growth on a hydrophobic substrate: learning from bivalve nacre, *CrystEngComm*, 22 (2020) 3100–3105.
- [8] N.M. Hwang, *Non–Classical Crystallization of Thin Films and Nanostructures in CVD and PVD Processes*, Springer Netherlands, 2016.
- [9] V.K. Ivanov, P.P. Fedorov, A.Y. Baranchikov, V.V. Osiko, Oriented attachment of particles: 100 years of investigations of non–classical crystal growth, *Russian Chemical Reviews*, 83 (2014) 1204–1222.

- [10] J.-S. Jung, S.-H. Lee, D.-S. Kim, K.-S. Kim, S.-W. Park, N.-M. Hwang, Non-classical crystallization of silicon thin films during hot wire chemical vapor deposition, *Journal of Crystal Growth*, 458 (2017) 8–15.
- [11] C. Lizandara-Pueyo, S. Dilger, M.R. Wagner, M. Gerigk, A. Hoffmann, S. Polarz, Li-doped ZnO nanorods with single-crystal quality – non-classical crystallization and self-assembly into mesoporous materials, *CrystEngComm*, 16 (2014) 1525–1531.
- [12] M. Niederberger, H. Cölfen, Oriented attachment and mesocrystals: Non-classical crystallization mechanisms based on nanoparticle assembly, *Physical Chemistry Chemical Physics*, 8 (2006) 3271–3287.
- [13] C. Rodríguez-Navarro, E. Ruiz-Agudo, J. Harris, S.E. Wolf, Nonclassical crystallization in vivo et in vitro (II): Nanogranular features in biomimetic minerals disclose a general colloid-mediated crystal growth mechanism, *Journal of Structural Biology*, 196 (2016) 260–287.
- [14] R. Song, T. Krasia-Christoforou, C. Debus, H. Cölfen, Structure and Magnetic Property Control of Copper Hydroxide Acetate by Non-Classical Crystallization, *Small*, 13 (2017) 1602702.
- [15] N.M. Hwang, D.Y. Yoon, Thermodynamic approach to the paradox of diamond formation with simultaneous graphite etching in the low pressure synthesis of diamond, *Journal of Crystal Growth*, 160 (1996) 98–103.
- [16] N.-M. Hwang, D.-Y. Kim, Charged clusters in thin film growth, *International Materials Reviews*, 49 (2004) 171–190.
- [17] K. Choi, S.-J.L. Kang, H.M. Jang, N.M. Hwang, Nucleation behavior in the presence of charge in the CVD diamond process, *Journal of Crystal Growth*, 172 (1997) 416–425.
- [18] H.M. Jang, N.M. Hwang, Theory of the charged cluster formation in the low pressure synthesis of diamond: Part I. Charge-induced nucleation, *Journal of Materials Research*, 13 (1998) 3527–3535.

- [19] H.M. Jang, N.M. Hwang, Theory of the charged cluster formation in the low pressure synthesis of diamond: Part II. Free energy function and thermodynamic stability, *Journal of Materials Research*, 13 (1998) 3536–3549.
- [20] N.M. Hwang, W.S. Cheong, D.Y. Yoon, Deposition behavior of Si on insulating and conducting substrates in the CVD process: approach by charged cluster model, *Journal of Crystal Growth*, 206 (1999) 177–186.
- [21] N.M. Hwang, Deposition and simultaneous etching of Si in the chemical vapor deposition (CVD) process: approach by the charged cluster model, *Journal of Crystal Growth*, 205 (1999) 59–63.
- [22] J.D. Jeon, C.J. Park, D.-Y. Kim, N.M. Hwang, Experimental confirmation of charged carbon clusters in the hot filament diamond reactor, *Journal of Crystal Growth*, 213 (2000) 79–82.
- [23] N.M. Hwang, W.S. Cheong, D.Y. Yoon, D.-Y. Kim, Growth of silicon nanowires by chemical vapor deposition: approach by charged cluster model, *Journal of Crystal Growth*, 218 (2000) 33–39.
- [24] J.-Y. Kim, D.-Y. Kim, N.-M. Hwang, Spontaneous generation of negatively charged clusters and their deposition as crystalline films during hot-wire silicon chemical vapor deposition, *Pure and Applied Chemistry*, 78 (2006) 1715–1722.
- [25] J.-H. Song, W. Jo, N.-M. Hwang, Non-uniform deposition in the early stage of hot-wire chemical vapor deposition of silicon: The charge effect approach, *Thin Solid Films*, 515 (2007) 7446–7450.
- [26] J.-I. Lee, N.-M. Hwang, Generation of negative-charge carriers in the gas phase and their contribution to the growth of carbon nanotubes during hot-filament chemical vapor deposition, *Carbon*, 46 (2008) 1588–1592.
- [27] C.-S. Kim, Y.-B. Chung, W.-K. Youn, N.-M. Hwang, Generation of charged nanoparticles during the synthesis of carbon nanotubes by chemical vapor deposition, *Carbon*, 47 (2009) 2511–2518.

- [28] S.Y. Park, S.M. Yang, C.S. Kim, N.M. Hwang, Effect of Bias Applied to Hot Wires on Generation of Positive and Negative Charges during Silicon Hot-Wire Chemical Vapor Deposition, *The Journal of Physical Chemistry C*, 113 (2009) 17011–17017.
- [29] N.-M. Hwang, D.-K. Lee, Charged nanoparticles in thin film and nanostructure growth by chemical vapour deposition, *Journal of Physics D: Applied Physics*, 43 (2010) 483001.
- [30] B.W. Clare, G. Talukder, P.J. Jennings, J.C.L. Cornish, G.T. Hefter, Effect of charge on bond strength in hydrogenated amorphous silicon, *Journal of Computational Chemistry*, 15 (1994) 644–652.
- [31] K. Kato, H. Omoto, T. Tomioka, A. Takamatsu, Visible and near infrared light absorbance of Ag thin films deposited on ZnO under layers by magnetron sputtering, *Solar Energy Materials and Solar Cells*, 95 (2011) 2352–2356.
- [32] K.-C. Lee, S.-J. Lin, C.-H. Lin, C.-S. Tsai, Y.-J. Lu, Size effect of Ag nanoparticles on surface plasmon resonance, *Surface and Coatings Technology*, 202 (2008) 5339–5342.
- [33] Y. Pan, Y. Fan, J. Niu, Optical properties of ultra-thin silver films deposited by thermal evaporation and its application in optical filters, *Infrared Physics & Technology*, 104 (2020).
- [34] H.K. Park, J.K. Yoon, K. Kim, Novel Fabrication of Ag Thin Film on Glass for Efficient Surface-Enhanced Raman Scattering, *Langmuir*, 22 (2006) 1626–1629.
- [35] S.H. Park, K.S. Lee, A. Sivasankar Reddy, Low emissivity Ag/Ta/glass multilayer thin films deposited by sputtering, *Journal of Applied Physics*, 110 (2011).
- [36] A. Bittner, H. Seidel, U. Schmid, Electromigration resistance and long term stability of textured silver thin films on LTCC, *Microelectronic Engineering*, 88 (2011) 127–130.
- [37] Y. Tsuda, H. Omoto, K. Tanaka, H. Ohsaki, The underlayer effects on the electrical resistivity of Ag thin film, *Thin Solid Films*, 502 (2006) 223–227.

[38] M. Guzman, J. Dille, S. Godet, Synthesis and antibacterial activity of silver nanoparticles against gram-positive and gram-negative bacteria, *Nanomedicine*, 8 (2012) 37–45.

[39] J.S. Kim, E. Kuk, K.N. Yu, J.H. Kim, S.J. Park, H.J. Lee, S.H. Kim, Y.K. Park, Y.H. Park, C.Y. Hwang, Y.K. Kim, Y.S. Lee, D.H. Jeong, M.H. Cho, Antimicrobial effects of silver nanoparticles, *Nanomedicine*, 3 (2007) 95–101.

[40] A.R. Shahverdi, A. Fakhimi, H.R. Shahverdi, S. Minaian, Synthesis and effect of silver nanoparticles on the antibacterial activity of different antibiotics against *Staphylococcus aureus* and *Escherichia coli*, *Nanomedicine*, 3 (2007) 168–171.

[41] I.-D. Jeon, D.-Y. Kim, N.-M. Hwang, Spontaneous generation of charged atoms or clusters during thermal evaporation of silver, *Zeitschrift für Metallkunde*, 96 (2005) 186–190.

[42] F. Hajakbari, M. Ensandoust, Study of Thermal Annealing Effect on the Properties of Silver Thin Films Prepared by DC Magnetron Sputtering, *Acta Physica Polonica A*, 129 (2016) 680–682.

[43] Y.S. Jung, Study on texture evolution and properties of silver thin films prepared by sputtering deposition, *Applied Surface Science*, 221 (2004) 281–287.

[44] N. Maréchal, E. Quesnel, Y. Pauleau, Silver thin films deposited by magnetron sputtering, *Thin Solid Films*, 241 (1994) 34–38.

[45] Y. Xiong, H. Wu, Y. Guo, Y. Sun, D. Yang, D. Da, Preparation and characterization of nanostructured silver thin films deposited by radio frequency magnetron sputtering, *Thin Solid Films*, 375 (2000) 300–303.

[46] K. Xu, L. Hao, M. Du, J. Mi, Q. Yu, S. Li, J. Wang, S. Li, Thermal emittance of Ag films deposited by magnetron sputtering, *Vacuum*, 174 (2020).

[47] O. Baghriche, A. Zertal, A.P. Ehiasarian, R. Sanjines, C. Pulgarin, E. Kusiak-Nejman, A.W. Morawski, J. Kiwi, Advantages of highly ionized pulse plasma magnetron sputtering (HIPIMS) of silver for

improved E. coli inactivation, *Thin Solid Films*, 520 (2012) 3567–3573.

[48] G.T. West, P.J. Kelly, J.W. Bradley, A Comparison of Thin Silver Films Grown Onto Zinc Oxide via Conventional Magnetron Sputtering and HiPIMS Deposition, *IEEE Transactions on Plasma Science*, 38 (2010) 3057–3061.

[49] A. Taden, K. Landfester, M. Antonietti, Crystallization of Dyes by Directed Aggregation of Colloidal Intermediates: A Model Case, *Langmuir*, 20 (2004) 957–961.

[50] D. Gebauer, A. Völkel, H. Cölfen, Stable Prenucleation Calcium Carbonate Clusters, *Science*, 322 (2008) 1819.

[51] B. Sadri, D. Pernitsky, M. Sadrzadeh, Aggregation and deposition of colloidal particles: Effect of surface properties of collector beads, *Colloids and Surfaces A: Physicochemical and Engineering Aspects*, 530 (2017) 46–52.

[52] S.–W. Park, J.–S. Jung, K.–S. Kim, K.–H. Kim, N.–M. Hwang, Effect of Bias Applied to the Substrate on the Low Temperature Growth of Silicon Epitaxial Films during RF–PECVD, *Crystal Growth & Design*, 18 (2018) 5816–5823.

[53] J.–H. Kwon, D.–Y. Kim, N.–M. Hwang, Generation of Charged Ti Nanoparticles and Their Deposition Behavior with a Substrate Bias during RF Magnetron Sputtering, *Coatings*, 10 (2020).

[54] B. Chapman, *Glow Discharge Processes: Sputtering and Plasma Etching*, Wiley, 1980.

[55] C. Igathinathane, L.O. Pordesimo, E.P. Columbus, W.D. Batchelor, S.R. Methuku, Shape identification and particles size distribution from basic shape parameters using ImageJ, *Computers and Electronics in Agriculture*, 63 (2008) 168–182.

[56] S. Iijima, T. Ichihashi, Structural instability of ultrafine particles of metals, *Physical Review Letters*, 56 (1986) 616–619.

[57] M. Zhang, M.Y. Efremov, F. Schiettekatte, E.A. Olson, A.T.

Kwan, S.L. Lai, T. Wisleder, J.E. Greene, L.H. Allen, Size-dependent melting point depression of nanostructures: Nanocalorimetric measurements, *Physical Review B*, 62 (2000) 10548–10557.

[58] D.B. Dove, Possible Influence of Electric Charge Effects on the Initial Growth Processes Occurring During the Vapor Deposition of Metal Films onto Substrates Inside the Electron Microscope, *Journal of Applied Physics*, 35 (1964) 2785–2786.

[59] F.T. Muniz, M.A. Miranda, C. Morilla Dos Santos, J.M. Sasaki, The Scherrer equation and the dynamical theory of X-ray diffraction, *Acta Crystallographica. section A, Foundations and Advances*, 72 (2016) 385–390.

[60] J.J. De Yoreo, P.U.P.A. Gilbert, N.A.J.M. Sommerdijk, R.L. Penn, S. Whitelam, D. Joester, H. Zhang, J.D. Rimer, A. Navrotsky, J.F. Banfield, A.F. Wallace, F.M. Michel, F.C. Meldrum, H. Cölfen, P.M. Dove, Crystallization by particle attachment in synthetic, biogenic, and geologic environments, *Science*, 349 (2015) aaa6760.

[61] H. Cölfen, *Mesocrystals and nonclassical crystallization*, Wiley England, 2008.

[62] M. Jehannin, A. Rao, H. Cölfen, New Horizons of Nonclassical Crystallization, *Journal of the American Chemical Society*, 141 (2019) 10120–10136.

[63] H.A. Abd El-Fattah, I. El-Mahallawi, M.H. Shazly, W.A. Khalifa, Microstructure Evolution of NiTi Magnetron Sputtered Thin Film on Different Substrates, *Key Engineering Materials*, 835 (2020) 68–74.

[64] D. Kim, D.Y. Kim, J.H. Kwon, K.-S. Kim, N.-M. Hwang, Generation of Charged SiC Nanoparticles During HWCVD Process, *Electronic Materials Letters*, 16 (2020) 498–505.

[65] W.-K. Youn, S.-S. Lee, J.-Y. Lee, C.-S. Kim, N.-M. Hwang, S. Iijima, Comparison of the Deposition Behavior of Charged Silicon Nanoparticles between Floating and Grounded Substrates, *The Journal of Physical Chemistry C*, 118 (2014) 11946–11953.

[66] S.-W. Park, G.-S. Jang, K.-S. Kim, N.-M. Hwang, Comparison

of Plasma Effect on Dewetting Kinetics of Sn Films Between Grounded and Floating Substrates, *Electronic Materials Letters*, 16 (2020) 72–80.

[67] N. Yamaguchi, Y. Sasajima, K. Terashima, T. Yoshida, Molecular dynamics study of cluster deposition in thermal plasma flash evaporation, *Thin Solid Films*, 345 (1999) 34–37.

[68] K. Terashima, Y. Norio, H. Tomoyuki, Y. Takamura, T. Yoshida, High rate deposition of thick epitaxial films by thermal plasma flash evaporation, *Pure and Applied Chemistry*, 70 (1998) 1193–1197.

[69] G.–S. Jang, D.–Y. Kim, N.–M. Hwang, The Effect of Charged Ag Nanoparticles on Thin Film Growth during DC Magnetron Sputtering, *Coatings*, 10 (2020).

[70] W. Bauer, G. Betz, H. Bangert, A. Bergauer, C. Eisenmenger-Sittner, Intrinsic resputtering during film deposition investigated by Monte Carlo simulation, *Journal of Vacuum Science & Technology A*, 12 (1994) 3157–3164.

[71] J. Chen, J. Suwardy, T. Subramani, W. Jevasuwan, T. Takei, K. Toko, T. Suemasu, N. Fukata, Control of grain size and crystallinity of poly-Si films on quartz by Al-induced crystallization, *CrystEngComm*, 19 (2017) 2305–2311.

[72] L.W. Rieth, P.H. Holloway, Influence of negative ion resputtering on ZnO:Al thin films, *Journal of Vacuum Science & Technology A*, 22 (2003) 20–29.

[73] I. Chakraborty, S.N. Shirodkar, S. Gohil, U.V. Waghmare, P. Ayyub, The nature of the structural phase transition from the hexagonal (4H) phase to the cubic (3C) phase of silver, *Journal of Physics: Condensed Matter*, 26 (2014) 115405.

[74] M.I. Novgorodova, A.I. Gorshkov, A.V. Mokhov, Native silver and its new structural modifications, *International Geology Review*, 23 (1981) 485–494.

[75] I.–D. Jeon, M.C. Barnes, D.–Y. Kim, N.M. Hwang, Origin of positive charging of nanometer-sized clusters generated during

thermal evaporation of copper, *Journal of Crystal Growth*, 247 (2003) 623–630.

[76] D. Grüner, Z. Shen, Ordered coalescence of nano-crystals during rapid solidification of ceramic melts, *CrystEngComm*, 13 (2011) 5303–5305.

[77] M. Hu, J.-S. Jiang, R.-P. Ji, Y. Zeng, Prussian Blue mesocrystals prepared by a facile hydrothermal method, *CrystEngComm*, 11 (2009) 2257–2259.

[78] M. Adachi, M. Kusumi, S. Tsukui, Ion-Induced Nucleation in Nanoparticle Synthesis by Ionization Chemical Vapor Deposition, *Aerosol Science and Technology*, 38 (2004) 496–505.

[79] J. Reiprich, N.A. Isaac, L. Schlag, T. Kups, M. Hopfeld, G. Ecke, T. Stauden, J. Pezoldt, H.O. Jacobs, Localized and Programmable Chemical Vapor Deposition Using an Electrically Charged and Guided Molecular Flux, *ACS Nano*, 14 (2020) 12885–12894.

[80] M. Wu, Y. Xu, L. Dai, T. Wang, X. Li, D. Wang, Y. Guo, K. Ding, X. Huang, J. Shi, J. Zhang, The Gas Nucleation Process Study of Anatase TiO₂ in Atmospheric Non-Thermal Plasma Enhanced Chemical Vapor Deposition, *Plasma Science and Technology*, 16 (2014) 32–36.

[81] H. Shirai, T. Kinoshita, M. Adachi, Patterning and Formation of SiO₂ Nanoparticles on a Substrate by Electrically Attracting of Cluster Ions, *Japanese Journal of Applied Physics*, 48 (2009) 070216.

[82] K. Nakaso, B. Han, K.H. Ahn, M. Choi, K. Okuyama, Synthesis of non-agglomerated nanoparticles by an electrospray assisted chemical vapor deposition (ES-CVD) method, *Journal of Aerosol Science*, 34 (2003) 869–881.

[83] C. Zhang, W. Ding, H. Wang, W. Chai, D. Ju, Influences of working pressure on properties for TiO₂ films deposited by DC pulse magnetron sputtering, *Journal of Environmental Sciences*, 21 (2009) 741–744.

국 문 초 록

직류 마그네트론 스퍼터링 공정 중 기상에서 하전된 은 나노 입자의 생성 가능성에 대한 연구를 하였다. 스퍼터된 은 입자는 투과 전자 현미경 (TEM) 관측을 위해 매우 얇은 비정질 탄소 분리막 위에 포집되었다. 기판에 양의 바이어스를 가했을 때 평균 입자 크기 및 증착된 입자의 총 면적이 기판에 음의 바이어스를 가했을 때 보다 더 큰 것을 확인 하였다. 결과는 스퍼터된 은 입자 중 일부가 음의 전하를 띠고 있음을 나타낸다. 박막 성장에 음으로 하전된 입자의 기여도를 확인하기 위해, 은 박막은 실리콘 기판에 -300 , 0 및 $+300$ V의 바이어스를 가하면서 30분동안 증착하였고, 전계 방출 주사 전자 현미경 (FESEM), X-선 회절 (XRD), 4-탐침법등을 이용하여 분석하였다. 기판에 $+300$ V의 바이어스가 인가되었을 때, 박막의 두께는 85.0 nm로 성장 속도가 가장 높았고, 0.44 의 가장 작은 반값폭과 가장 낮은 $3.67 \mu\Omega \cdot \text{cm}$ 의 비저항을 가져 최고의 결정성을 보였다. 반대로, 기판에 -300 V의 바이어스가 인가되었을 때, 박막의 두께는 68.9 nm로 성장 속도가 가장 낮았고, 0.53 의 가장 큰 반값폭과 가장 큰 $8.87 \mu\Omega \cdot \text{cm}$ 의 비저항을 가져 최저의 결정성을 보였다. 이 결과는 하전이 박막 성장에 중요한 역할을 하며 DC 마그네트론 스퍼터링에서 새로운 공정 변수가 될 수 있음을 나타낸다.

하전된 나노 입자에 대한 공정 변수의 영향을 연구하기 위해 직류 (DC) 마그네트론 스퍼터링 중 은 박막의 증착 속도 및 미세 구조, 결정성 및 전기적 특성에 대한 스퍼터링 전력의 영향을 조사하였다. 100 nm 두께의 은 박막은 10, 20, 50, 100 및 200 W의 스퍼터링 전력으로 증착되었고, FESEM, XRD, TEM과 4-탐침법을 이용하여 분석하였다. 10 W의 스퍼터링 전력으로 증착된 은 박막은 가장 낮은 성장 속도를 보이지만 가장 낮은 반값폭과 가장 낮은 비저항으로 가장 높은 결정성을 보였다. 200 W의 스퍼터링 전력으로 증착된 은 박막은 가장 높은 성장률을 가지며 반값폭 및 비저항이 두 번째로 낮아 두 번째로 높은 결정성을 보였다. 50 W의 스퍼터링 전력으로 증착된 은 박막은 중간 정도의 성장률을 가지며 최악의 결정성을 보였다. 고 분해능 TEM 관찰 결과, 스퍼터링 파워 10 및 200 W로 증착된 은 박막은 50 W의 스퍼터링 파워로 증착된 은 박막에 비해 입자 경계, 전위 및 적층 결함과 같은 결함이 훨씬 적었다. 이러한 증착 거동은 스퍼터링 파워가 나노 입자 사이즈에 영향을 주어 하전된 나노 입자 생성에 영향을 미치는 것으로 설명할 수 있다. 그리고 증착 속도가 매우 빠른 조건에서 좋은 품질의 박막을 얻을 수 있으며, 이 때 하전이 매우 중요한 역할을 하게 된다.

그리고 DC 마그네트론 스퍼터링의 공정 압력이 은 박막의 두께, 결정성 및 전기적 특성에 미치는 영향을 조사하였다. 20, 50, 100 및 200 W의 플라즈마 전력과 2.5, 5, 10 및 20 mTorr의 공정 압력에서 30분

동안 -300 , 0 및 $+300$ V의 바이어스를 기판에 가하면서 박막을 증착하였다. 실험 결과 모든 스퍼터링 파워 조건에서 공정 압력이 감소할수록 박막의 성장 속도가 증가하고 하전된 나노 입자의 비율이 증가하였다. 또한 기판에 양의 바이어스를 가했을 때 박막의 성장 속도는 증가하였고, 기판에 음의 바이어스를 가했을 때 박막의 성장 속도는 감소하였다. XRD 분석을 통해 얻은 은의 (111) 면의 반값폭은 공정 압력이 감소할 때 기판에 가해진 바이어스에 따라 다른 양상을 보였다. 기판에 양의 바이어스를 가했을 때, 반값폭은 감소하였고, 기판에 음의 바이어스를 가했을 때, 반값폭은 증가하였다. 전기적 특성을 확인하기 위해 측정한 비저항 역시 반값폭과 같은 변화 양상을 보였다. 이러한 은 박막의 증착 거동의 변화는 하전된 나노 입자의 영향으로 이해할 수 있다. 공정 압력이 나노 입자의 크기를 변화시켰고, 이렇게 나노 입자의 사이즈 차이가 하전 가능성을 달라지게 만든다. 이렇게 생긴 하전된 나노 입자는 박막 성장에 큰 영향을 주게 된다. 따라서 하전이 박막 성장 거동에 매우 중요한 역할을 한다고 할 수 있다.